Charge Delocalization in the Special-Pair Radical Cation of Mutant Reaction Centers of *Rhodobacter sphaeroides* from Stark Spectra and Nonadiabatic Spectral Simulations

Pakorn Kanchanawong,[†,§] Mats G. Dahlbom,[‡] Thomas P. Treynor,[§] Jeffrey R. Reimers,*[,‡] Noel S. Hush,[‡,||] and Steven G. Boxer*[,§]

Biophysics Program and Department of Chemistry, Stanford University, Stanford, California, 94305-5080, and Schools of Chemistry and Molecular and Microbial Sciences, The University of Sydney, Sydney, New South Wales 2006, Australia

Received: April 18, 2006; In Final Form: July 13, 2006

Stark and absorption spectra for the hole-transfer band of the bacteriochlorophyll special pair in the wild-type and L131LH, M160LH, and L131LH/M160LH mutants of the bacterial reaction center of *Rhodobacter sphaeroides* are presented, along with extensive analyses based on nonadiabatic spectral simulations. Dramatic changes in the Stark spectra are induced by the mutations, changes that are readily interpreted in terms of the redox-energy asymmetry and degree of charge localization in the special-pair radical cation. The effect of mutagenesis on key properties such as the electronic coupling within the special pair and the reorganization energy associated with intervalence hole transfer are determined for the first time. Results for the L131LH and M160LH/L131LH mutants indicate that these species can be considered as influencing the special pair primarily through modulation of the redox asymmetry, as is usually conceptualized, but M160LH is shown to develop a wide range of effects that can be interpreted in terms of significant mutation-induced structural changes in and around the special pair. The nonadiabatic spectra simulations are performed using both a simple two-state 1-mode and an extensive four-state 70-mode model, which includes the descriptions of additional electronic states and explicitly treats the major vibrational modes involved. Excellent agreement between the two simulation approaches is obtained. The simple model is shown to reproduce key features of the Stark effect of the main intervalence transition, while the extensive model quantitatively reproduces most features of the observed spectra for both the electronic and the phase-phonon regions, thus giving a more comprehensive description of the effect of the mutations on the properties of the special-pair radical cation. These results for a series of closely related mixed-valence complexes show that the Stark spectra provide a sensitive indicator for the properties of the mixed-valence complexes and should serve as an instructive example on the application of nonadiabatic simulations to the study of mixed-valence complexes in general as well as other chemical systems akin to the photosynthetic special pair.

I. Introduction

Primary charge separation during bacterial photosynthesis is initiated at the *special pair* P of bacteriochlorophyll (BChl) molecules in the photosynthetic reaction center (RC).[1] The individual molecules in this dimer are named P_L and P_M after the protein chains to which their magnesium atoms are ligated. Optical energy absorbed by peripheral light-harvesting proteins is funneled to P, which then ejects an electron to initiate the primary charge separation, leaving behind a dimer radical cation P^+. The electron hole thus produced may be either localized on one of the two halves, fully delocalized over both, or some state in between.[2−6] The electrochemical properties of the reaction centers are very sensitive to the nature of this charge partitioning;[7−12] the understanding of such effects forms a significant aspect of research into energy capture in both natural photosystems and proposed devices aimed at harvesting and using solar energy.

Historically, the most revealing experimental techniques for understanding the special pair and its electronic properties have involved combinations of site-directed mutagenesis,[13−15] Fourier transform infrared (FTIR) spectroscopy,[16−18] and electron paramagnetic resonance (EPR) and electron nuclear double resonance (ENDOR) spectroscopy.[7−10,19,20] Mutagenesis studies, guided by X-ray structural data,[21−24] have allowed controlled environmental modification of the properties of the special pair, with the assumption that changes to a single amino acid residue affect primarily the local structure and electrostatics. ENDOR spectroscopy reveals the spin densities on selected atoms in the BChl molecules from which the fraction of the positive charge localized on each moiety can be directly deduced. FTIR spectroscopy not only reveals key changes in hydrogen-bond patterns induced by mutations through observed changes to chromophores vibrational frequencies but also measures the *electronic* absorption spectra arising from the very low energy transitions that are uniquely available to the dimer radical cation. The assignment of these transitions to particular electronic states,[25,26] the fitting of experimental spectra,[4,5] and the extraction of key chemical data from these spectral analyses have led to a comprehensive model describing the charge-localization,

* Authors to whom correspondence should be addressed. E-mail: reimers@chem.usyd.edu.au; sboxer@stanford.edu.
[†] Biophysics Program, Stanford University.
[‡] School of Chemistry, The University of Sydney.
[§] Department of Chemistry, Stanford University.
[||] School of Molecular and Microbial Biosciences, The University of Sydney.

10.1021/jp0623894 CCC: $33.50
Published on Web 08/30/2006

spectroscopic, and electrochemical properties of the special-pair radical cation.[12]

Recently, Stark spectroscopy[27−32] has been used to evaluate the nature of the charge localization[4,33] in a variety of mixed-valence systems, including the mid-infrared band of the special-pair radical cation in the wild-type (WT) reaction center of *Rhodobacter* (*Rb.*) *sphaeroides*.[28] In this study, we measure the absorption and Stark spectra for the WT and L131LH, M160LH, and M160LH/L131LH mutants[15,17,19] of *Rb. sphaeroides*; the three representative mutants are selected on the premise that they should induce dramatic changes to the Stark spectra. We describe the theoretical foundation for the spectroscopic and chemical modeling of the special-pair radical cation in section II. The experimental methods are described in section III. Both the absorption and the Stark spectra are presented in section IV. In section V, the observed spectra are analyzed by first comparing to a priori predictions based on the existing[5,12] nonadiabatic model. The simulations are then further refined to quantitatively reproduce the observed data, providing detailed information concerning both local and nonlocal effects of the mutations. These are compared to a spectroscopic model using a minimal set of variable parameters[4] that is shown to reproduce most of the qualitative features of the spectra, further verifying the appropriateness of the basic analysis.

II. Theoretical Background

A. Description of the Hole-Transfer Transition. The spectra of the special-pair radical cations show many unique features that are not present in the spectra of either the neutral special-pair dimer or the corresponding monomer radical cation species. This includes, for example, some of the most intense vibrational lines in the FTIR spectrum, lines arising from modes of pseudo-*g* symmetry on each porphyrinic macrocycle.[34,35] These transitions are known as *phase-phonon* lines.[36] Also, a range of intense low-lying electronic transitions arise including the hole-transfer (HT) band, second-highest occupied molecular orbital (SHOMO) to highest occupied molecular orbital (HOMO) band[26] (SH), and tripdoublet bands.[25,30] Viewed in the localized description in which the cation radical (hole) is assumed to reside on just one of the dimer halves, the HT band involves simply moving the hole to the other half, e.g., $P_L^+P_M \rightarrow P_LP_M^+$, similar to the intervalence band[37,38] observed in a typical inorganic mixed-valence complex (MVC) such as the Creutz−Taube ion.[39] The SH transition is allowed for monomer radical cations but for porphyrinic systems is very weak and not observable, whereas in porphyrinic dimer radical cations it can be quite intense.[30,34] Tripdoublet bands involve singlet-to-triplet excitations of the neutral half, a process forbidden in the monomer akin to phosphorescence, which becomes spin-allowed and dramatically enhanced in the presence of the nearby radical cation.[40] In addition, bands arising from multiple excitations can occur, a significant one being the double excitation HTSH involving HT from one monomer to the other followed by SH on the monomer that becomes neutral.[5,35] For *Rb. sphaeroides*, the HT, SH, and tripdoublet bands have been identified in the spectra: The HT band appears as a broad transition with a long high-frequency tail centered at ca. 2700 cm^{-1},[16,41] the SH band appears[26] at 2200 cm^{-1} as a shoulder of the HT band, and the tripdoublet band appears at ca. 8000 cm^{-1} and closely parallels the monomer phosphorescence.[42] Intensification of the phase-phonon lines in the vibrational part of the spectrum arises due to strong vibronic coupling with the HT band,[25] producing the rather unusual vibrational spectrum of the dimer radical cation.

As typical of MVCs, the spectroscopic and chemical properties of the dimer radical cation are strongly influenced by the nature of the charge localization/delocalization between the two halves. In the simplest conceptual approach, only the ground state (GS) and HT state need be considered. Figure 1 shows potential-energy surfaces for these two states of the bacterial RC special pair, sketched as a function of a generalized antisymmetric vibrational coordinate that interpolates between the geometries of the fully charge-localized $P_L^+P_M$ and $P_LP_M^+$ systems. Shown are the localized diabatic potential-energy surfaces (solid) and the Born−Oppenheimer adiabatic surfaces (dashed) that result from coupling between the localized states. While modern chemistry is usually conceptualized in terms of Born−Oppenheimer adiabatic surfaces, in this case, the diabatic ones are easier to model and manipulate in general nonadiabatic approaches. The key parameters controlling the interaction are shown in the figure; these are the reorganization energy $\lambda^{A,GS-HT}$, the electronic coupling J^{GS-HT}, and the redox asymmetry E_0^{GS-HT}. The dimer radical cation is a particular example of a MVC in which optically driven electron transfer causes the interchange of the valence states of a pair of redox centers. Considered separately from its environment, the BChl homodimer comprising the special pair is a symmetric system; however, interactions with the protein induce differences in the structure and environment of each chromophore. These factors are accounted for in this model through the redox asymmetry parameter, E_0^{GS-HT}, that depicts the driving force for hole transfer from one of the BChls to the other.

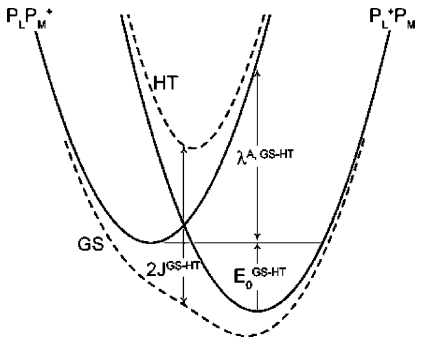

Figure 1. Ground state and hole-transfer state for the special-pair radical cation of *Rb. sphaeroides* as depicted through the localized diabatic ($P_L^+P_M$ and $P_LP_M^+$) and adiabatic (GS and HT) representations of the potential-energy surfaces.

An alternate description of MVCs can be constructed in terms of delocalized diabatic states.[5,35] In this picture, the electronic coupling is assumed to be the dominant factor so that the charge becomes equally spread over both chromophores. As the adiabatic potential-energy surfaces depicting the special-pair radical cation shown in Figure 1 each have a single minimum, this diabatic picture is in fact the most appropriate one. (Alternatively, the lower surface could have a double-minimum structure.[5,39]) The electronic states then take on the symmetry properties of the assumed symmetric dimer: For bacterial photosynthesis, this symmetry is C_2, and the delocalized diabatic states are named ^{2}B (predicted by calculations to be the ground state) and ^{2}A (the hole-transfer state). One additional feature of the problem that becomes readily apparent in the delocalized diabatic picture is the effect of the symmetric vibrational modes on the system; these act to give different geometries for the ^{2}B and ^{2}A states, giving a coordinate dependence[3,5,6,28] to the otherwise assumed coordinate-independent electronic coupling J^{GS-HT}. In the localized diabatic approach, this is know as a non-Condon effect, and its inclusion is critical for the description of the spectroscopy of the system in regions dominated by strong coupling. The simplest parameter describing this effect is the symmetric-mode reorganization energy $\lambda^{S,GS-HT}$ depicting the

energy associated with relaxation processes between the structures for the ^{2}B and ^{2}A states.[34] However, as the contributions from low-frequency symmetric vibrations are efficiently treated using a general Gaussian broadening contribution to the spectrum, we choose to explicitly include only modes of frequency >200 cm^{-1}, and so replace $\lambda^{S,GS-HT}$ with its high-frequency component $\lambda^{S200,GS-HT}$ during the analysis.[5]

A practical method for determining the spectral and chemical properties of symmetric MVCs involving just antisymmetric vibrational processes was first developed by Piepho, Krausz, and Schatz (the PKS model).[43] Their method has now been extended to include both antisymmetric and symmetric vibrational modes as well as asymmetric dimers.[3−6,12] More generally, such approaches involve the solutions of *vibronic coupling* problems,[44] ones that involve couplings between the motion of the atoms and the nature of the electronic wave functions. However, as the SH absorption overlaps the HT band in the spectra of bacterial reaction centers,[26] we have enhanced the above two-state model through the inclusion of the SH and HTSH states.[5] This increases the number of major parameters in the model from 4 (J^{GS-HT}, E_0^{GS-HT}, $\lambda^{A,GS-HT}$, and $\lambda^{S,GS-HT}$) to 10, the new parameters being directly analogous ones $J^{SH-HTSH}$, $E_0^{SH-HTSH}$, and $\lambda^{A,SH-HTSH}$ for the SH/HTSH pair, the relative energy of the SH and GS states E_{SH}, and cross reorganization energies $\lambda^{A,HT-SH}$ and $\lambda^{A,GS-HTSH}$.

However, insufficient unique information is contained[7,8] in the observed absorption spectrum alone to determine all 6 of these new parameters as the SH state appears only as a shoulder while HTSH is a dark state. Hence, in a previous study,[5] the assumption was introduced that the SH−HTSH interaction directly paralleled the GS−HT one, i.e., $J^{SH-HTSH} = J^{GS-HT}$, $E_0^{SH-HTSH} = E_0^{GS-HT}$, $\lambda^{A,SH-HTSH} = \lambda^{A,GS-HT}$, and $\lambda^{A,GS-HTSH} = \lambda^{A,HT-SH}$, leaving only two new parameters, the energy gap E_{SH} and the reorganization energy normalizing the vibronic coupling between the HT and SH states, $\lambda^{A,GS-SH}$. These two parameters control the location and intensity of the SH shoulder and are readily determined from the observed spectra. Here, through incorporation of the Stark spectra into the analysis, unique values for $\lambda^{A,SH-HTSH}$ and $E_0^{SH-HTSH}$ are also determined. These parameters adjust the degree of charge localization in the SH/HTSH states and the penetration of the SH state under HT.

Practical computational methods require not only the total reorganization energies but also their distribution among the appropriate normal modes of vibration. We take two approaches in dealing with this issue. First, we use a comprehensive partitioning based on the results of density functional calculations for the special-pair radical cation.[35] This involves the use of the 50 most significant antisymmetric modes and the 20 most significant symmetric ones and all 4 electronic states. Second, we take the minimalist approach and take just one effective antisymmetric vibrational mode and include only the GS and HT states. This approach captures the essential features of the absorption, Stark, and spin-resonance spectroscopies of MVCs.[3,4,11,33] The entire solution space of the model has been mapped previously,[3] and like in the case of the comprehensive model, the absorption spectra alone do not provide sufficient information to determine unique values for all of the parameters. Here again unique parameters may be obtained[4] by simultaneously fitting both the absorption and the Stark spectra. While the latter model clearly can neither describe features such as the highly structured phase-phonon bands that arise from each specific mode involved nor the properties of the 2200 cm^{-1} shoulder, it involves many fewer parameters and hence, as a matter of principle, is less susceptible to yielding erroneous solutions. Furthermore, from a more general standpoint, the spectra for the phase-phonon bands of typical MVCs are difficult to either measure and assign or accurately compute a priori, but the absorption and Stark spectra of the higher-energy electronic component can be readily measured for many MVCs, and these are remarkably insensitive to the nature of the vibrational partitioning.[38] As a result, the simpler two-state model should be of general utility in the characterization of MVC systems including those that do not lend themselves to high-resolution analysis. This study should thus form an instructive example for future applications of Stark spectroscopy to characterize MVC systems.

B. Stark Spectroscopy of Mixed-Valence Complexes. Since the first application of Stark spectroscopy to an inorganic MVC,[29] namely, the Creutz−Taube ion, the technique has become one of the key tools in the characterization of MVCs, and it has been customary to analyze the Stark spectra using the model developed by Liptay.[45] Recently, however, a theory for Stark spectroscopy for MVCs has been developed, based on nonadiabatic simulations in the context of the two-state model, and the serious shortcomings of the Liptay model have been demonstrated.[4,33] The conceptual differences between the two approaches are summarized here to outline the key features. The Liptay model[45] (alternatively called the classical Stark model) is based on the assumption that the transition energy $h\nu$ for a particular immobilized molecule can be expanded as

$$h\nu(\mathbf{F}) = h\nu(0) - f\mathbf{F}\cdot\Delta\mu - \frac{f^2\mathbf{F}\cdot\Delta\alpha\cdot\mathbf{F}}{2} \qquad (1)$$

where $\mathbf{F}$ is the applied electric field vector, $\Delta\mu$ and $\Delta\alpha$ are the changes in dipole moment and polarizability upon absorption, respectively, and f is the local-field correction factor ($1 < f < 1.3$).[46] For an isotropic ensemble of immobilized molecules, analytical expressions for the Stark spectroscopy can be derived as a sum of terms proportional to the absorption band shape (zeroth derivative), its first derivative, and its second derivative (see Appendix). The coefficients of these terms are directly related to electro-optic parameters of the molecules: The zeroth derivative component is governed by the polarizabilities (A) and hyperpolarizabilities (B) of the transition dipole moment ($\vec{m}$), the first-derivative component by both $\Delta\alpha$ and a cross-term involving $\Delta\mu$ and A and the second-derivative component by the magnitude of $\Delta\mu$. In applications to MVCs, $\Delta\mu$ has been related to the effective charge-transfer distance and is expected to be the dominant property[29,33,47] for a highly localized system, so large second-derivative responses are to be expected.

Equation 1, which underpins the classical Liptay analysis, is based on the adiabatic theory, however, and as such is not strictly applicable to MVCs.[4,33] A more general relation that must be used is

$$E_0^{GS-HT}(\mathbf{F}) = E_0^{GS-HT}(0) - \frac{f\mathbf{F}\cdot\Delta\mu - f^2\mathbf{F}\cdot\Delta\alpha\cdot\mathbf{F}}{2} \qquad (2)$$

in which, rather than perturbing the transition energy directly as in eq 1, the electric field operates on the term E_0^{GS-HT}, the energy asymmetry or the driving force of the charge-transfer reaction. For charge-transfer systems, $|\Delta\mu|$ is large, directly proportional to the effective charge-transfer distance between the diabatic states, $\Delta\mu = e\cdot\mathbf{r}_{CT}$, while $\Delta\alpha = 0$ for symmetric systems and so it is usual[4,33] to truncate eq 2 at the linear term, ignoring the effects of asymmetry on $\Delta\alpha$, and indeed we adopt this practice herein. In the limit where the corresponding energy

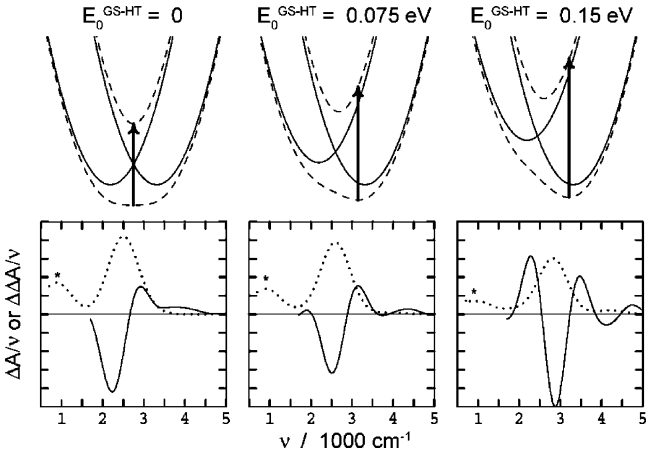

Figure 2. Calculated effect of redox asymmetry on absorption and Stark spectrum line shapes. The top frames show sample localized diabatic (—) and adiabatic (- -) potential-energy surfaces for a series of MVCs akin to the bacterial photosynthetic reaction center with redox asymmetries E_0^{GS-HT} of 0, 0.075 (600 cm^{-1}), and 0.15 eV (1200 cm^{-1}) obtained using $J^{GS-HT} = 0.136$ eV (1100 cm^{-1}), $\lambda^{A,HT-GS} = 0.136$ eV (1100 cm^{-1}), vibration frequency $\nu = 1200$ cm^{-1}, and Gaussian resolution 700 cm^{-1}; arrows mark the Born−Oppenheimer Franck−Condon vertical excitation energies. The lower panels show the corresponding open-shell (e.g., P^+) minus closed-shell (e.g., P) absorption spectra $\Delta A/\nu$ (dots) and Stark spectra $\Delta\Delta A/\nu$ (—) predicted in each case. The asterisks indicate the phase-phonon lines. (These become sharp at high resolution.)

gap E_0 is much larger than the coupling J or reorganization energy λ, the frequency of the transition $h\nu \approx E_0$, the spectroscopy of the MVC approaches that of ordinary ground to excited state transitions, and thus Liptay's equations hold. The situation is more complicated for the strongly coupled, delocalized MVCs where $E_0 \approx 0$,[12] since the frequency of the transition does not respond to the field in a linear fashion. Instead, as illustrated in Figure 2 and described in detail later, the $\mathbf{F}\cdot\Delta\mu$ term leads to an increase in transition energy for every orientation of the molecules, mimicking the effect of $\Delta\alpha$ in the classical Liptay theory.[4,28] In the limit of weakly coupled MVC ($2|J| < \lambda$), the lower adiabatic state becomes double-welled, and if $2|J| \ll \lambda$, then the tunneling between the wells becomes slow on the spectroscopic time scale, leading[38] to $h\nu \approx E_0 + \lambda$, and the electric field response simplifies to that of eq 1, and Liptay's analysis is appropriate. In terms of the Stark line shape, the Stark spectra are expected to be dominated by the second-derivative line shape for both the large E_0 limit[4] and the weakly coupled, charge-localized scenario.[33] The magnitude of $\Delta\mu$ can be inferred directly from the observed Stark spectra, and this is one of the most common applications of Stark spectroscopy.[29,48,49] However, meaningful fit parameters for $\Delta\mu$ cannot be determined from the Liptay analysis of the delocalized or intermediate cases.[4,33] Instead a quantitative interpretation of the Stark spectra of MVCs requires a full nonadiabatic analysis general enough to account for both the limiting cases and the intermediate cases.[4,5,12,33] These and a range of other effects, i.e., the dependence of the spectral line shape and the population on the electric field, can induce non-Liptay behaviors (generally called nonclassical Stark effects) and have been considered in detail elsewhere.[4,50,51]

C. Application to the Special-Pair Radical Cation (P^+). Treynor, Andrews, and Boxer[28] have measured the intervalence band absorption and Stark spectra of WT P^+ and presented a two-state 1-mode analysis, while Reimers and Hush[5] have analyzed their absorption spectrum using four-state 70-mode model. Both analyses returned very similar results of $J^{GS-HT} =$ 0.136/0.126 eV, $\lambda^{A,GS-HT} =$ 0.136/0.139 eV, and $E_0^{GS-HT} =$ 0.075/0.069 eV for the two-state/four-state approaches, respectively. Treynor et al.[28] also extracted $\Delta\mu$ from the Stark spectrum, obtaining 32 D/*f* from the two-state 1-mode vibronic analysis, while Reimers and Hush used density functional theory (DFT) calculations[12] to predict 34 D/*f*, demonstrating that this value leads to an accurate *prediction* of the Stark spectrum. These results thus support the validity of the central premises of the vibronic coupling approach and the applicability of both the comprehensive and the simple models used. However, through the use of classical Liptay analysis, the value of 8.2 D/*f* for $\Delta\mu$ was obtained,[28] revealing the shortcomings of the classical approach.

In this study, the light minus dark difference absorption and Stark spectra for the RCs, $\Delta A(\nu)$ and $\Delta\Delta A(\nu)$, are measured directly as the spectra for the illuminated reaction less that for the nonilluminated one and are dominated by processes occurring on the special pair. The L131LH, M160LH, and M160LH/L131LH mutants are chosen since they modulate hydrogen bonding to the 13^1-keto groups of the P_L and P_M BChls, groups that are in conjugation with the macrocyclic π-systems. L131LH replaces leucine with histidine to add a hydrogen bond to P_L, whereas M160LH adds the analogous hydrogen bond to P_M. These changes affect the redox potentials of the two halves, as it is more difficult to oxidize macrocycles that accept hydrogen bonds, thus directly modulating E_0^{GS-HT}. In addition, if the hydrogen bonding responds to excitations on the spectroscopic time scale, then these mutations also directly modulate the reorganization energy $\lambda^{A,GS-HT}$. Primarily through these changes, mutations thus modify the charge delocalization and hence all chemical and spectroscopic properties of the special-pair radical cation.[7−12] Indirect effects of the mutations are also possible, for example, the modulation of J^{GS-HT} and $\Delta\mu$, through perturbations in the structure or the alignment of the two pigments within the special pair.

Significant changes to the FTIR absorption and Stark spectra of the dimer cations are anticipated[7−12] to arise from mutations introduced near the 13^1-keto positions of the BChls primarily through their modulation of E_0^{GS-HT}. The qualitative origin of this effect is illustrated in Figure 2 using the two-state 1-mode model, with $J^{GS-HT} = 0.136$ eV, $\lambda^{A,GS-HT} = 0.136$ eV, and a frequency of 1200 cm^{-1} for the antisymmetric vibrational mode. This figure shows the localized diabatic and adiabatic potential-energy surfaces for a symmetric special-pair-type MVC ($E_0 = 0$) and ones with asymmetries of $E_0^{GS-HT} = 0.075$ and 0.15 eV, respectively. Induced changes in the absorption spectra for this series can be demonstrated by applying the Franck−Condon approximation to the vertical transition between the adiabatic surfaces. Due to a good Franck−Condon overlap, the symmetric MVC ($E_0^{GS-HT} = 0$) absorbs strongly at an electronic band-origin maximum of ca. 2600 cm^{-1}, displaying both a vibrational progression to high energy and also a phase-phonon line at 900 cm^{-1}. (Note that the phase-phonon line is depressed somewhat from the diabatic vibration frequency of 1200 cm^{-1} due to the very strong vibronic coupling concentrated in just one vibrational mode and that *all* the spectral features shown in this figure are broadened to the low resolution typical of an electronic transition whereas phase-phonon lines actually have sub-cm^{-1} resolution.) When $E_0^{GS-HT} > 0$, the maximum of the intervalence absorption band increases in frequency, the reduction in Franck−Condon overlap decreases the absorption intensity and increases the bandwidth, and the phase-phonon line significantly weakens due to the reduced interaction between the electronic states. The fraction of the charge delocalized on P_L, ρ_L, obtained for the

three values of E_0^{GS-HT} used are 50% (0 eV), 67% (0.075 eV), and 79% (0.15 eV), values that span the common range[11,12] of observed spin localizations produced by mutants of *Rb. sphaeroides*. This diagram is thus expected to qualitatively indicate the key effects of mutation on the absorption spectra.[4,12] Also shown in the figure are the predicted Stark spectra for each scenario. The delocalized case gives a first-derivative-shaped spectrum with one zero-crossing, while $E_0^{GS-HT} = 0.15$ eV produces a second-derivative-shaped response with two zero-crossings associated with the central band region. The variations in the Stark line shapes can be seen to be much more dramatic than the variations in the absorption spectra and even at a qualitative level provide a strong indication of the variations in the redox asymmetry and the degree of charge delocalization in P^+.

III. Materials and Methods

A. Site-Directed Mutagenesis. Site-directed mutagenesis of the L and M genes was performed using oligonucleotide-directed mutagenesis kit from Stratagene (QuikChange). The desired mutations on the pufL and pufM genes were verified by sequencing the gene fragments inserted into the pRKSCH plasmid, which was constructed for the expression of polyhistidine-tagged RCs.[52] The mutant pRKSCH plasmids were then conjugated into the ΔLM1.1 strain of *Rb. sphaeroides*.[15,53] The cells were grown semi-aerobically in the dark for 6−7 days. The purification of RCs from harvested cells using Ni−NTA resin and anion exchange chromatography has been described elsewhere.[52] The purified RCs were exchanged into a Tris/Triton X-100 buffer (10 mM Tris, 0.1% Triton X-100, pH 8.0) and concentrated in a Centricon YM-30 centrifugal filter device (Millipore).

B. FTIR Spectra. A Bruker IFS66v/s FTIR spectrometer with a Globar light source and a KBr beam splitter was used, equipped with either a liquid-nitrogen-cooled InSb detector for absorption and Stark measurements in the 1800−5000 cm^{-1} range or a liquid-nitrogen-cooled mercury cadmium telluride (MCT) or a noncooled deuterated tri-glycine sulfate (DTGS) detector for the 700−5500 cm^{-1} range. Spectra were taken with 4 cm^{-1} resolution. Samples were cooled to 77 K in a liquid nitrogen immersion cryostat[54] fitted with ClearTran inner windows and CaF_2 outer windows (for Stark experiments) or ZnS inner windows and KBr outer windows (for absorption in the 700−5500 cm^{-1} range). The exposure of the sample to the actinic beam, supplied by a 600 W tungsten−halogen source and filtered by a water filter, is controlled by an electronic shutter. Light above 5500 cm^{-1} was blocked by a germanium filter placed in front of the detector.

Light-induced difference spectra (ΔA) were obtained from interferograms taken prior to, during, and after illumination, as described by Breton.[18] The magnitudes of the absorption spectra were not observed to decrease over time as in previous experiments,[28] and spectra from hundreds of cycles of illumination were averaged to improve the signal-to-noise ratio. The Stark spectra were taken by the synchronized AC method whereby the voltage applied to the sample is turned on and off at alternate interferogram sampling points.[55] This modulation scheme is necessary to eliminate the baseline roll caused by low-frequency fluctuation during a particular leg of mirror travel. The phase of the applied voltage is shifted by $\pi/2$ for adjacent interferogram scans so that a pair of interferograms can be recombined to yield a field-on and a field-off interferogram. The field-off spectrum was subtracted from the field-on spectrum to give the Stark spectrum. The light-off Stark spectrum was subtracted from the light-on Stark spectrum to yield the Stark spectrum of the light-induced difference spectrum ($\Delta\Delta A$). The electric field waveform synchronous to the FTIR sampling was generated by a controller designed in-house[55] and multiplied 1000 times by a TREK 10/10 high-voltage amplifier (TREK, Inc., Medina, NY). Stark spectra were taken with the sample perpendicular to the IR beam ($\chi = 90°$).

Nonlinear response of the photoconductive MCT detectors can give rise to baseline distortions for the $P^+Q_A^-$ minus PQ_A difference spectra. A DTGS detector that has good linear response was used, following the work of Clerici et al.,[18] to determine the correct line shape for the absorption spectra for the 700−5500 cm^{-1} range. Spectra taken with the more sensitive MCT detector were compared to the spectra taken by the DTGS detector, and the baseline distortion was corrected by polynomial functions. The correction is not perfect, however, for spectra in the 700−1800 cm^{-1} range that contain many sharp features. In subsequent analyses the experimental spectra are broadened by 300 cm^{-1}, and the error due to incomplete baseline correction is thus minimized. For the 1800−5000 cm^{-1} range, the photovoltaic InSb detector exhibits good linear response, and the absorption and Stark spectra are not corrected. The spectra measured by the DTGS and the InSb detectors are in good agreement.

C. Sample Preparation. Samples for absorption measurement were prepared by depositing a small amount (0.8−1.2 μL) of concentrated RC solution onto an ice-cooled ZnS or ZnSe window. The RCs were partially dried by a gentle stream of N_2, and another window was placed on the dehydrated film. Samples for Stark spectroscopy were prepared similarly on Ni-coated sapphire windows (~40−60 Å of Ni deposited by evaporation). The nickel layers serve as semitransparent electrodes, allowing the electric field to be applied to the sample.

Three approaches were used in assembling the Stark cells. In the first, the nickel layers were patterned so that only a small area in the center of the assembled cell constitutes the electrode pairs. The RCs were deposited to cover this area completely, and the area outside of the capacitor cavity is masked. This type of Stark sample is modeled as a parallel plate capacitor with a uniform electric field in the cavity. The magnitude of the applied electric field is calculated from the applied voltage and the thickness of the sample cell determined mechanically by a digital micrometer with an accuracy of ±2 μm or ca. 10%. Samples prepared this way support smaller electric fields and yield Stark spectra with lower signal-to-noise ratios. However, the magnitude of the Stark effect is more accurately determined because the sample is homogeneous. The magnitudes of the Stark spectra of P^+ in RC mutants scale as the square of the applied field (vide infra), as has been observed for WT P^+.[28]

The second approach allows higher signal-to-noise ratio Stark spectra to be obtained by increasing the maximum applied voltage the sample can withstand to up to 4 kV. A thin film of Teflon (12.5 μm nominal thickness) was inserted into the sample between the RC film and one of the Ni-coated windows, and a small amount of perfluorinated vacuum grease (Krytox, Dow Corning), which has no significant absorption in the 1800−5000 cm^{-1} range, was applied to fill in the gap as necessary. This procedure effectively enhances the dielectric strength of the sample, allowing for a high effective field across the protein, with a significant improvement in the signal-to-noise ratio of the Stark spectra. Because the sample is inhomogeneous, consisting of two materials with different dielectric constants, the effective electric field is not determined accurately. The Stark spectra obtained were scaled based on the results from the first type of cell where the magnitude is determined more accurately.

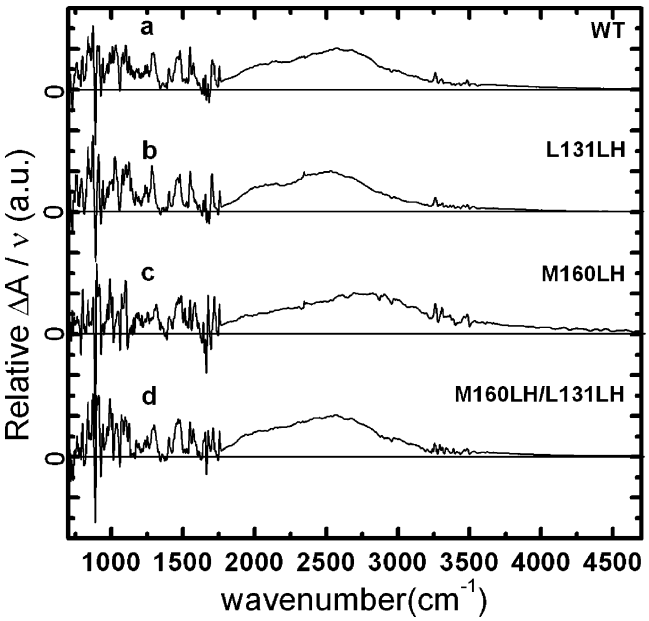

Figure 3. Observed light minus dark (oxidized versus neutral) difference absorption spectra ΔA (displayed as frequency-weighted spectra, $\Delta A/\nu$) for RCs of (a) the WT and the mutants (b) L131LH, (c) M160LH, and (d) M160LH/L131LH of *Rb. sphaeroides* at 77 K in the range of 700−4700 cm^{-1} obtained using a MCT/DTGS detector combination. The spectra are normalized so that the peaks of the intervalence band in the 2500−3000 cm^{-1} range have the same intensity.

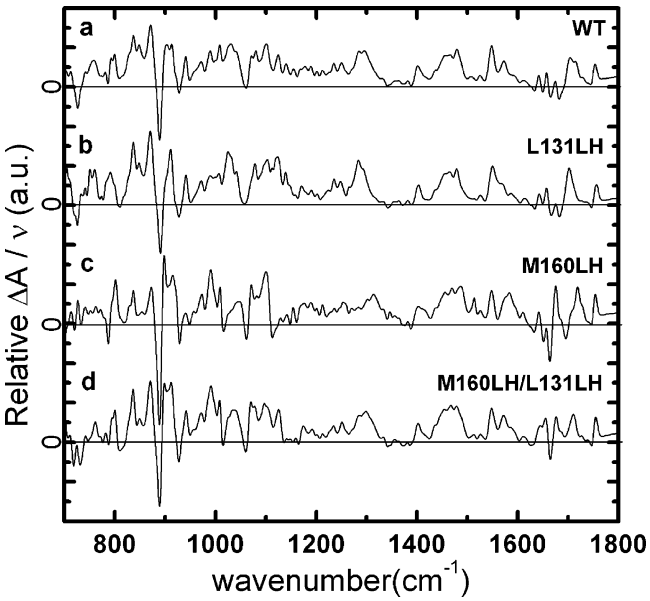

Figure 4. Observed light minus dark (oxidized versus neutral) difference absorption spectra ΔA (displayed as frequency-weighted spectra, $\Delta A/\nu$) for RCs of (a) the WT and the mutants (b) L131LH, (c) M160LH, and (d) M160LH/L131LH of *Rb. sphaeroides* at 77 K in the phase-phonon region (700−1800 cm^{-1}) obtained using a DTGS detector. The spectra are normalized as in Figure 3.

In the third approach, the Stark cell was preassembled from a pair of Ni-coated sapphire windows and Teflon spacers (25 μm nominal thickness). The thickness of the cell is determined to high accuracy from the interference fringes of the empty cell. The sample in 1:1 buffer/glycerol is then injected into the cell, which is rapidly frozen upon insertion into the cryostat. The thickness is measured more precisely, but the solvent obscures large sections of the spectra in the mid-IR. Because the intervalence band spectra of RC in frozen glycerol/buffer glass are slightly different from the dehydrated spectra, this approach primarily serves as a qualitative estimate. The magnitudes of the Stark spectra for the hydrated sample were observed to be very similar to those of dehydrated samples for all the mutants. This technique thus constitutes an independent verification of the earlier estimates of the film thickness.

D. Determining the Magnitude of the Electric Field Strength. The applied field ($\mathbf{F}_{applied}$) is calculated from the applied voltage ($V_{applied}$) and the measured path length of the cell (d) using the parallel plate model: $\mathbf{F}_{applied} = V_{applied}/d$. $\mathbf{F}_{applied}$ is assumed to be macroscopically uniform. However, the effective field inside the protein can be modulated by the local-field correction factor f through the assumed scalar form: $\mathbf{F}_{effective} = f\mathbf{F}_{applied}$. The correction factor f is estimated to be 1.0−1.3 for protein interiors.[46] This factor is difficult to determine experimentally and was explicitly left as a scalar factor for electric-field-dependent parameters. The maximum applied field of 1.05 MV cm^{-1} is achieved in samples with a Teflon film inserted.

IV. Experimental Results

A. IR Absorption Spectra of Mutant RCs. The light-induced difference spectra for the WT and mutant RCs in the 700−4700 cm^{-1} range are shown in Figure 3, with the 700−1800 cm^{-1} range highlighted in Figure 4. At 77 K, the light-induced difference spectra correspond primarily to the $P^+Q_A^-$ intermediate. (Q_B is typically highly depleted in the protocol used, and $Q_A^- \rightarrow Q_B$ electron transfer is inhibited at low temperature.[56]) The intervalence bands are observed as a broad peak in the 1750−5000 cm^{-1} range. (For a more detailed view, see the top panels of Figure 5.) Below 1750 cm^{-1}, multiple sharp negative and differential signals are observed. These pairs of negative and positive peaks, denoted as −/+, reflect peak shifts upon photooxidiation of the special pair. The cluster of sharp bands observed in the 3200−3600 cm^{-1} region is likely due to N−H and O−H stretching frequencies that shift upon P^+ formation; small sharp features at around 2900 cm^{-1} are due to the C−H modes in the protein background. The maximum amplitudes of the difference spectra for the mutant RCs are on the order of 0.01−0.04 absorbance units; for comparison, the spectra are normalized so that the peak of the intervalence band is unity. As has been observed for WT RCs,[28] the spectra of the intervalence band in dehydrated samples are shifted toward lower energy by several tens of cm^{-1} in the mutants relative to that of the RCs in a buffer/glycerol glass (data not shown).

The peak frequencies, average frequencies, and standard deviations of the intervalence bands (1800−5000 cm^{-1}) are listed in Table 1. The intervalence band spectra for the WT is very similar to that measured by Breton and co-workers previously,[17] with a maximum at 2600 cm^{-1}, a long tail extending toward high frequency, and a shoulder at around 2200 cm^{-1} due to the SH transition. For the L131LH RC, the peak of the intervalence band shifts down to 2508 cm^{-1}. The band is slightly narrower with increased intensity in the shoulder. For M160LH RC, the intervalence band broadens appreciably with the peak moving to 2751 cm^{-1}; the shoulder is significantly diminished and merges into the main intervalence band. In the double mutant, the peak of the intervalence band, at 2514 cm^{-1}, is at a lower energy relative to WT, the band is broader, and the shoulder is more prominent. In comparison to previously published spectra of the mutants,[17] which were measured for chromatophore membrane samples, the intervalence band spectra

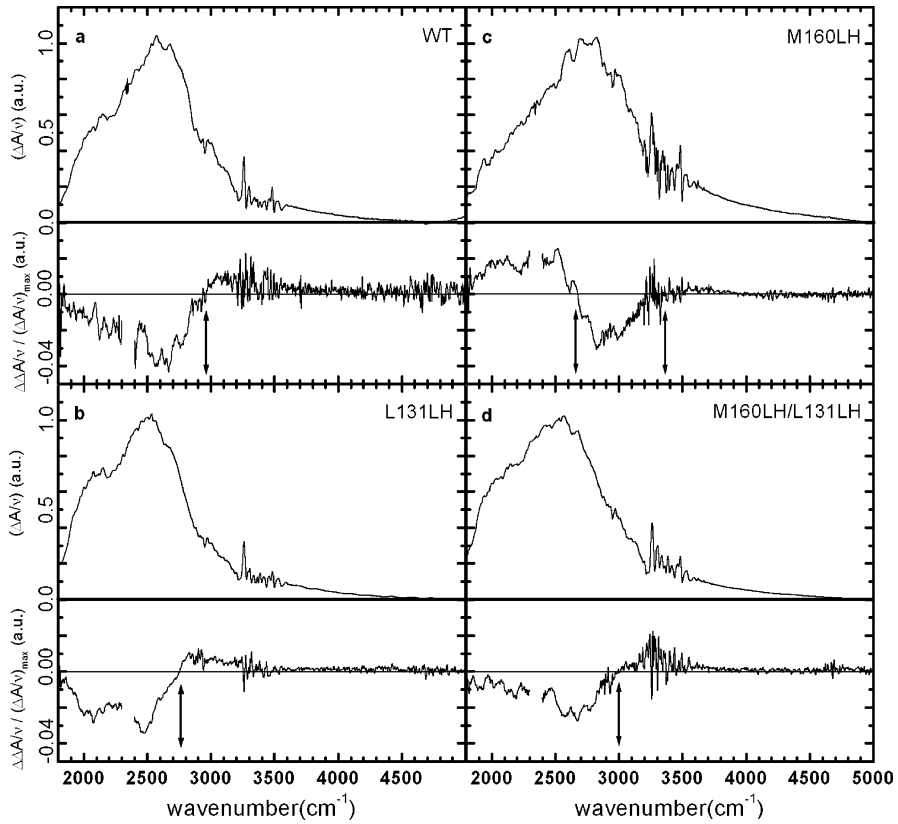

Figure 5. Observed Stark spectra $\Delta\Delta A$ (bottom panels), normalized with the light minus dark (oxidized versus neutral) difference absorption spectra ΔA (top panels, normalized to unity) for RCs of (a) the WT and the mutants (b) L131LH, (c) M160LH, and (d) M160LH/L131LH of *Rb. sphaeroides* at 77 K in the range of 1800−5000 cm^{-1} obtained using an InSb detector. The spectra displayed are frequency-weighted ($\Delta A/\nu$ and $\Delta\Delta A/\nu$). The Stark spectra are normalized to the maximum intensity of the absorption spectra as well as to the electric field strength of 1 MV/cm. The arrows indicate the frequencies of the zero-crossing points.

TABLE 1: Properties of the Observed Light Minus Dark (Oxidized Minus Neutral) Absorption Spectra of the WT of *Rb. Sphaeroides* and Its Mutants in the 1800−5000 cm^{-1} Region, Including the Average[a] and Standard Deviation[b] of the Bandshape Function A/ν

species	absorption maximum (cm^{-1})	average (cm^{-1})	standard deviation (cm^{-1})
WT	2593	2647	495
L131LH	2508	2599	512
M160LH	2751	2891	665
M160LH/L131LH	2514	2613	527

[a] Average $= \int A(\nu)\, d\nu / \int A(\nu)\nu^{-1}\, d\nu$. [b] Standard deviation $= (\int(\nu - \text{average})^2 A(\nu)\nu^{-1}\, d\nu / \int A(\nu)\nu^{-1}\, d\nu)^{(1/2)}$.

are qualitatively similar with the changes relative to the WT following the same trend.

The special-pair BChls contain several carbonyl groups absorbing in the 1620−1760 cm^{-1} range whose frequencies upshift upon photooxidation, appearing as differential peaks in the difference spectra shown in Figure 4. Notable differences are observed for the 13^1-keto carbonyl frequencies in the mutants as the introduced histidines in L131LH and M160LH were designed to donate hydrogen bonds to these carbonyl groups. The observed frequencies and their changes on oxidation are summarized in Table 2, while conclusions drawn concerning the nature of the hydrogen bonding (further discussed in subsection V.D) are presented in Table 3. In the WT, no hydrogen bonding to the 13^1-keto carbonyl group is involved, and the differential peaks at 1682(−)/1705(+) cm^{-1} with shoulders at 1689(−)/1714(+) cm^{-1} have been assigned to the free 13^1-keto carbonyl groups of P_M and P_L, respectively.[17] For

TABLE 2: Observed 13^1-Keto Vibration Frequencies for the Neutral RCs ν_-, Oxidized RCs ν_+, and Their Difference $\Delta\nu = \nu_+ - \nu_-$, in cm^{-1}

	P_L			P_M		
species	ν_-	ν_+	$\Delta\nu$	ν_-	ν_+	$\Delta\nu$
WT	1689	1714	25	1682	1705	23
L131LH	1682	1701	19	1682	1701	19
M160LH	1695	1718	23	1663	1676	13
L131LH/M160LH	1664?[a]	1711	47?[a]	1664	1676	12

[a] An alternate assignment at $\nu_- = 1693$ cm^{-1} and $\Delta\nu = 18$ cm^{-1} would indicate that no hydrogen bond at all forms to P_L, but this appears inconsistent with the observed Stark spectrum.

TABLE 3: Nature of the Hydrogen Bonding to the 13^1-Keto Groups of the Special Pair in Its Neutral Form P, Equilibrated GS Radical Cation P^+, and Vertically Excited HT Radical Cation P^+ Form

	P_L			P_M		
species	P	GS	HT	P	GS	HT
WT						
L131LH	weak[a]	weak	weakened			
M160LH				strong	strong	broken
L131LH/M160LH	strong	broken	broken	strong	strong	weakened

[a] A hydrogen bond could form to the 13^3-ester group rather than the 13^1-keto one.

the L131LH mutant, a single differential signal at 1682(−)/1701(+) cm^{-1} is observed. This is in contrast to the chromatophore spectra of this mutant as observed by Nabedryk et al.,[17] in which multiple small peaks are observed in this region. These are interpreted as arising from the overlap between the positive peak of the hydrogen-bonded 13^1-keto carbonyl of P_L in P^+

and the negative peak of 13^1-keto carbonyl of P_M in neutral P.[17] It has been observed that two different 13^1-keto spectral signatures can result from different preparation conditions or in combination with other mutations; the downshifted peak position, as tentatively observed for the chromatophore samples,[17] indicates strong hydrogen bonding, while the relatively higher-frequency peak observed here for the purified RC indicates a weak bonding. It has been suggested[57] that this situation arises as the introduced histidine in L131LH mutants is somewhat distant from the 13^1-keto group and is also in close proximity to the adjacent 13^3-ester group, allowing for the possibility of competitive hydrogen-bonding processes. For the M160LH mutant, two sets of differential peaks are observed at 1695(−)/1718(+) cm^{-1} due to the free 13^1-keto carbonyl of P_L and at 1663(−)/1676(+) cm^{-1} due to the hydrogen-bonded 13^1-keto carbonyl of P_M,[17] similar to those observed in the chromatophore membrane by Nabedryk et al.[17] These results indicate that this mutant forms strong hydrogen bonds to P_M in both neutral and oxidized reaction centers.

The spectra of the double mutant M160LH/L131LH shows differential peaks at 1664(−)/1676(+) cm^{-1}, indicating that the 13^1-keto carbonyl of P_M is strongly hydrogen-bonded to the M160 histidine for both P and P^+. A positive peak is also observed at 1711 cm^{-1} that is attributed to P_L; while the associated negative peak may be the weak signal observed at 1693 cm^{-1}, it is more consistent with the observed spin-density and electrochemical data to presume instead that it is at the same frequency as that of P_L, 1664 cm^{-1}. This interpretation indicates that a strong hydrogen bond forms also to the 13^1-keto group of neutral P_L that is broken upon oxidation; the significant qualitative difference between this scenario and the hydrogen bonding to the 13^1-keto group of P_L in the L131LH mutant has been noted previously.[57] In the chromatophore spectra of Nabedryk et al.,[17] large differential peaks at 1662(−)/1685(+)cm^{-1} were observed and interpreted as arising from the 13^1-keto carbonyls of both P_L and P_M, which form hydrogen bonds to the L131 and M160 histidines, respectively. Hence it is clear that sample preparation does influence the strengths of the hydrogen bonds in this species.

For all RCs, differential peaks attributable to at least one 13^3-ester group at 1745(−)/1753(+) cm^{-1} are observed.[17] Similarly, the 3^1-acetyl groups can be assigned to the differential peaks at 1637(−)/1641(+) cm^{-1} and 1651(−)/1658(+) cm^{-1}.[17] However, the strong amide I band of the protein overlaps with the 3^1-acetyl frequencies, and assignments are tentative.[17]

In the low-frequency spectra, positive bands at around 1300, 1450, and 1550 cm^{-1} have been identified as distinct phase-phonon transitions, corresponding to vibrational modes activated by intervalence electron transfer.[17] Phase-phonon intensity throughout the entire region is also manifested through many differential peaks whose positive component is much stronger than the negative one.[5] The strong negative peaks at 727 and 889 cm^{-1} in the WT spectra correspond to modes observed in resonance Raman spectra of P.[58] The negative peak at 1061 cm^{-1} has been attributed to a C−N stretch of neutral P based on an ^{15}N isotope substitution experiment, although the specific origin of this mode has not been assigned.[59] Interestingly, this peak appears to split for the M160LH and M160LH/L131LH mutants.

B. Stark Spectra of Mutant RCs. The energy-weighted absorption and Stark spectra in the 1800−5000 cm^{-1} range are shown in Figure 5. The Stark spectra in the bottom panels are conormalized with the absorption spectra and scaled to a field strength of 1 MV cm^{-1} for comparison. The magnitudes of the Stark spectra for all mutants were observed to scale quadratically with the applied electric field (data not shown). The spectral region between 2300 and 2400 cm^{-1} is obscured by the absorption of liquid nitrogen in the immersion cryostat and is omitted from the display. Strong absorption of the C−H, O−H, and N−H stretches of the protein and the remaining solvent strongly attenuate the measuring beam in the 2900−3000 and 3200−3600 cm^{-1} windows, giving rise to phase error and higher noise in the Stark spectra; the signal-to-noise ratios are improved by extensive signal averaging. As has been observed in the WT,[28] the Stark spectra for the dehydrated film samples are qualitatively similar to the frozen hydrated sample in both line shape and magnitude but with a shift toward lower energy of several tens of cm^{-1} similar to that observed for the absorption (data not shown). The Stark spectra for the 1200−1800 cm^{-1} window containing the phase-phonon bands has been previously described for the WT and shows no significant assignable features.[28] Similar results are observed for the mutants (data not shown). In the previous study of the WT RCs, the peak intensity for the dehydrated film was observed to slowly decrease under strong illumination by 5−10%;[28] this was not observed for the dehydrated RC films studied here.

The Stark spectrum for the WT is largely negative with a zero-crossing at 2950 cm^{-1}, on the high-energy side of the intervalence band maximum, and small positive intensity for the long high-frequency tail of the spectra. For the Stark spectra of L131LH, the zero-crossing is at 2746 cm^{-1}, closer to the maximum of the intervalence band. The low-energy side of the spectrum is negative with small positive intensity for the long high-frequency tail. The negative amplitude for the shoulder sideband on the low-energy side is prominent. For M160LH, the Stark line shape is drastically different from the other RCs, showing a zero-crossing on both sides of the maximum of the intervalence band, a strong positive feature on the low-energy side, and a very small positive feature for the high-frequency tail of the spectrum. Also, a positive feature due to the shoulder sideband can be observed at around 2100 cm^{-1}. For the double mutant M160LH/L131LH, the Stark spectrum is qualitatively very similar to the WT but with a smaller amplitude.

C. Artifacts in Absorption and Stark Spectra. The nearly saturating absorption of the protein and the solvent constitutes a source of experimental error. A small phase error for the sharp spectral features in the background gives rise to an incomplete background subtraction in the difference spectra. This can result in artificial peaks where the background strongly absorbs and obscures the signal in the difference spectra; for example, the 3^1-acetyl stretches overlap with the amide I band (1660 cm^{-1}) and were obscured by a false peak in the M160LH/L131LH spectra. This error is limited to small regions of the spectra and does not affect the overall shape of the absorption spectra appreciably. However, for the Stark spectra, this effect gives rise to a significant level of noise in the 3200−3600 cm^{-1} range due to strong background absorption from the N−H and O−H stretch modes. The spectral quality is improved by averaging over multiple samples and for long times. In the Stark spectra there are also other noticeable artifacts such as the residual interference fringes (e.g., in the Stark spectrum for M160LH in Figure 5), which originate from interferences of the probe beam and the beam internally reflected within the sample. The interference fringes do not completely cancel out in the difference spectra because of the unequal attenuation due to the absorption of P^+ present during illumination.

V. Spectral Modeling

A. Predicting and Fitting the Spectral Data. The simulation methodology for the four-state 70-mode model and the two-state 1-mode model for WT P^+ has been described in detail elsewhere.[4−6,12] In an effort to understand the effects of the mutations on the properties of P^+, simulations were initially performed with strict parameter constraints, which were progressively relaxed to obtain an optimized fit to the observed spectra, as described in the following. For the four-state 70-mode model, the parameter values for WT have been determined from fitting the absorption spectra in conjunction with modeling the dependence of midpoint potential on charge localization for 25 mutant RCs;[12] this parameter set is henceforth referred to as WT(previous). In the first set of calculations, which we call a priori prediction, the absorption and Stark spectra of the mutant RCs are calculated with all the model parameters constrained to those of WT(previous) with the exception of the energy asymmetry E_0^{GS-HT}, for which the values predicted[12] by spin-density and the electrochemical potential of P have been used. Next, the model parameters are allowed to vary to fit just the absorption spectra for the mutants, with the Stark spectra calculated accordingly and scaled to fit the observed spectra by varying the $\Delta\mu$ parameter (model 4/70A). In the third set, the model parameters are optimized to simultaneously fit both the absorption and the Stark spectra (model 4/70A&S). For the two-state 1-mode model (model 2/1A&S), simultaneous fits to both the absorption and the Stark spectra are performed using the central region of the hole-transfer absorption band. The precise spectral ranges (ca. 2300−3000 cm^{-1}) used in the two-state 1-mode fits are given in Table 4; this region excludes the 2200 cm^{-1} shoulder caused by the SH state as well as the high-frequency tail and phase-phonon regions of the spectra that are sensitive to the detailed descriptions of the vibrational modes. The fit parameters from all the simulations are given in Table 4 while the calculated and observed absorption and Stark spectra are compared in Figure 6. Note that all these computational approaches use the same underlying mathematical formulations as described in our previous studies[4,5,12] but differ in the choices of unconstrained fit parameters, the targets for spectral optimization, and/or the numbers of vibronic states included. This approach is chosen to dissect the contribution of individual parameters to the fit quality and as a way to analyze the sensitivity of the model to various input. The error estimates and the model limitations for each case are then discussed in this and the following subsections. Alternatively, calculations could be performed at the highest level, that is, 4/70A&S, with the errors estimated using standard methods. With an eye toward further improving the implementation of the model for other mixed-valence complexes, we thus adopt the current approach of sensitivity analysis for its instructive value.

From the results of these fits, spin densities on P_L, ρ_L, and electrochemical midpoint potential changes ΔE_m are calculated and given in Table 5, along with the changes in dipole moment between the localized diabatic states, $\Delta\mu$, determined from the magnitude of the Stark spectra. To evaluate the midpoint potentials, the specification of the effects of each mutation on both the P_L and the P_M halves is required. An earlier analysis[12] indicates that this can be represented by a ratio η of the distances of the mutation site to the center of each cofactor; the value of $\eta = 0.18$ was obtained from an optimization to fit the data for 25 mutants[12] and was used in this study. The observed absorption spectra are smoothed to 300 cm^{-1} resolution before fitting while the Stark spectra are broadened to 50 cm^{-1} resolution. This broadening not only reduces noise but also

TABLE 4: Parameters, in eV, from Previous Analyses[5,28] of the WT (Used to Predict the Absorption and Stark Spectra of Mutants) and New Sets Optimized Using the Four-State 70-Mode Model Fitting to the Absorption Spectra (4/70A) or the Absorption and Stark Spectra (4/70A&S) and the Two-State 1-Mode Model (2/1A&S) Fitting to the Absorption and Stark Spectra[a−d]

	J^{GS-HT}			$\lambda^{A,GS-HT}$			E_0^{GS-HT}			$\lambda^{S200,GS-HT}$			$\lambda^{A,HT-SH}$		E_{SH}		$\lambda^{A,SH-HTSH}$	$E_0^{SH-HTSH}$
mutant	4/70A	4/70A&S	2/1A&S	4/70A	4/70A&S	2/1A&S	4/70A	4/70A&S	2/1A&S	4/70A	4/70A&S	2/1A&S	4/70A	4/70A&S	4/70A	4/70A&S	4/70A&S	4/70A&S
WT(previous)	0.126		0.136	0.139		0.136	0.069[e]		0.075	0.0027		0.095	0.071		0.180			
WT	0.126	0.128	0.134	0.136	0.129	0.118	0.079	0.083	0.095	0.0057	0.0060	0.095	0.076	0.077	0.181	0.196	0.318	0.061
L131LH	0.121	0.120	0.132	0.167	0.173	0.131	−0.026	−0.043	−0.066	0.0076	0.0089	0.199	0.095	0.095	0.181	0.190	0.285	0.001
M160LH	0.101	0.095	0.107	0.214	0.198	0.153	0.152	0.176	0.199	0.0052	0.0046	0.063	0.063	0.056	0.180	0.168	0.340	0.146
M160LH/L131LH	0.118	0.119	0.119	0.161	0.147	0.124	0.070	0.083	0.130	0.0024	0.0046	0.076	0.076	0.081	0.181	0.197	0.346	0.065

[a] The spectral simulations do not determine the sign of E_0^{GS-HT}; the signs most consistent with the experimental midpoint potentials and spin densities from Table 5 are shown. [b] The SHOMO to HOMO interaction parameters $\lambda^{A,SH-HTSH}$ and $E_0^{SH-HTSH}$ are set equal to $\lambda^{A,GS-HT}$ and E_0^{GS-HT}, respectively, in the 4/70A analyses, while $J^{SH-HTSH}$ and $\lambda^{A,GS-HTSH}$ are set to J^{GS-HT} and $\lambda^{A,SH-HTSH}$, respectively, throughout. [c] All 4/70A and 4/70A&S spectra are determined to 300 cm^{-1} resolution, while the resolution is optimized to fit the 2/1A&S spectra, obtaining 721 cm^{-1} (WT), 594 cm^{-1} (L131LH), and 679 cm^{-1} (M160LH and M160LH/L131LH). [d] The 2/1A&S spectra are fitted only in the central region of 2250 cm^{-1} (WT), 2300 cm^{-1} (L131LH), 2400 cm^{-1} (M160LH and M160LH/L131LH) $< \nu <$ 3000 cm^{-1}. [e] Values[12] used for the mutants are −0.011 eV (L131LH), 0.168 eV (M160LH), and 0.069 eV (M160LH/L131LH).

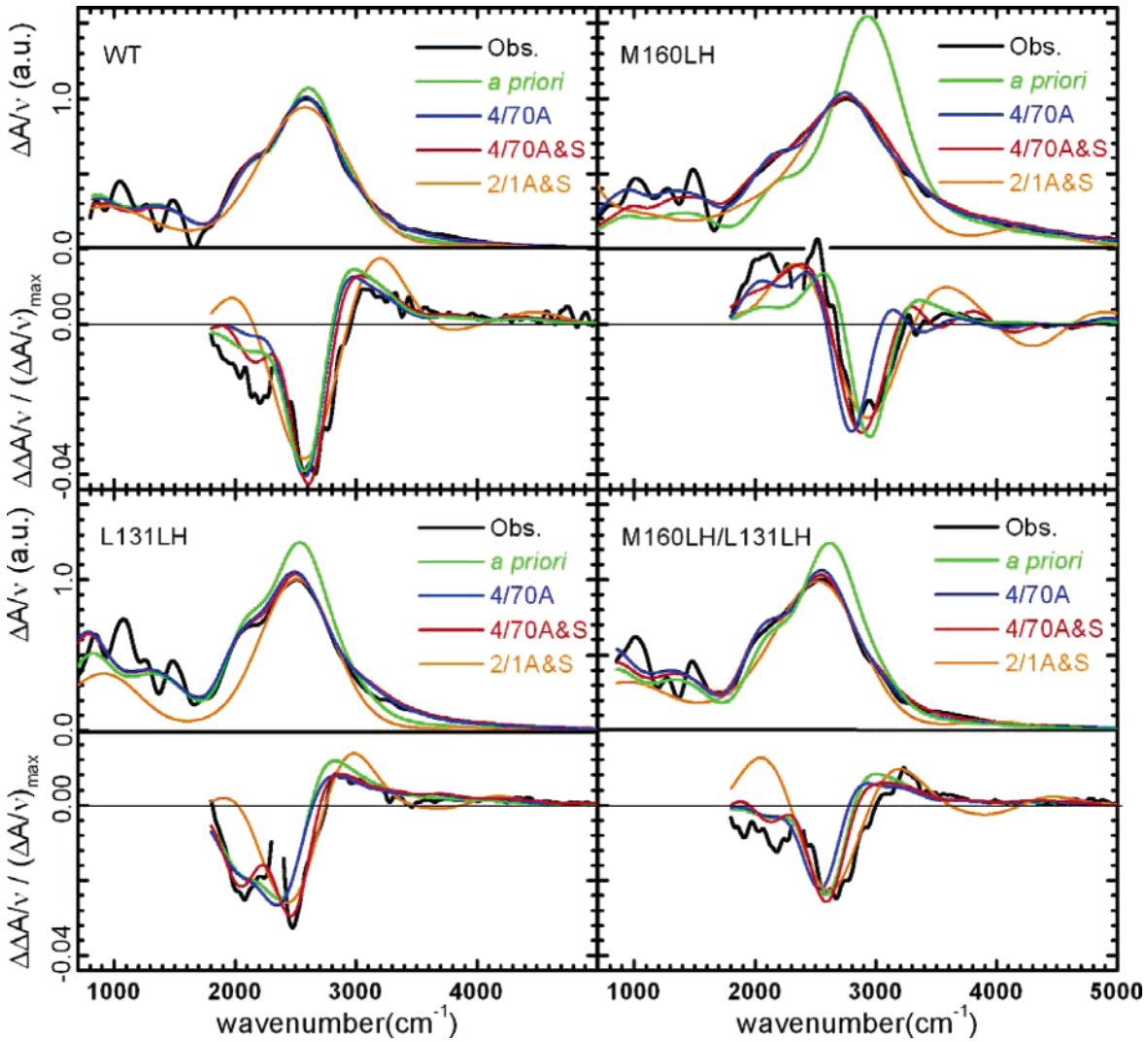

Figure 6. Comparison of observed light minus dark (cation minus neutral) difference spectra ΔA and Stark spectra $\Delta\Delta A$ (black) with predicted spectra based on a previous a priori analysis[5] of the WT (green), fitted spectra using the 4/70A model (blue), fitted spectra using the 4/70A&S model (red), and fitted spectra using the 2/1A&S model (orange). For the 4/70A model, the four-state 70-mode model is used with only the observed absorption spectra as the optimization targets and with the magnitude of the Stark spectra scaled to fit the observed spectra by varying $\Delta\mu$. For the 4/70A&S model, the four-state 70-mode model is used to fit to both the observed absorption and the Stark spectra simultaneously. For the 2/1A&S model, the two-state 1-mode model is used with the spectra fitted to only the central region of both absorption and Stark spectra (Table 4). For clarity, the observed spectra are broadened to 100 cm^{-1} resolution (absorption) and 50 cm^{-1} resolution (Stark). The spectra displayed are frequency-weighted ($\Delta A/\nu$ and $\Delta\Delta A/\nu$). The Stark spectra are normalized by the maximum intensity to the absorption spectra as well as to the electric field strength of 1 MV/cm. The calculated spectra are normalized so as to facilitate comparison of the Stark line shape, which contains more distinguishing features than the absorption spectra.

clarifies the absorption spectra by eliminating the large differential effects observed in the vibrational region of the spectra. These features are associated with vibrational transitions whose frequencies change upon charge separation. As a result, the net intensity gain in the low-frequency region due to the activation of phase-phonon lines[36] and its broad distribution are clearly exposed for comparison to that predicted using the model.

As shown in Figure 5, a key feature of the experimental results is the dramatic difference of the Stark line shape among the mutants. The hydrogen-bond mutations used in this study are expected to induce significant changes in the energy asymmetry parameter E_0^{GS-HT} causing a subsequent variation in the Stark line shape. The observed changes in the Stark spectra as shown in Figure 5 agree quite well with predictions from even the simple two-state 1-mode model,[4] illustrated in Figure 2. However, while the changes in E_0^{GS-HT} clearly dominate the global appearance of the Stark line shape, changes in other parameters are also present, as will be discussed in the remainder of this section. One of the useful criteria for the description of the Stark line shape adopted herein is the position and the number of the Stark zero-crossing point(s). This provides a useful visual guide to the quality of the overall fit to the observed spectra as the position and number of these zero-crossings serves as a convenient point of reference for distinguishing different types of line shapes. For example, for a purely first-derivative type line shape, the single Stark zero-crossing is at the frequency of the band maximum, while for the purely second-derivative type line shape, two Stark zero-crossings are present, each on both sides of the band maximum.

With regard to previous calculations for WT, the values of the parameters optimized herein for WT using the 4/70A&S and 2/1A&S simulations agree very well.[5,12,28] The minor differences in the 4/70A analysis are largely a result of the extended range (700−5000 cm^{-1}) of the observed spectra in this study, while the small differences in the fit parameters for

TABLE 5: Spin Densities ρ_L on P_L, Changes in Midpoint Potential ΔE_m, and Changes in Dipole Moment between the Localized Diabatic States $P_L^+P_M$ and $P_LP_M^+$, as Deduced from the Spectra Fits, from Previous Analyses[5,28] of the WT (Used to Predict the Absorption and Stark Spectra of Mutants), and from the New Sets Optimized Using the Four-State 70-Mode Model Fitting to the Absorption Spectra (4/70A) or the Absorption and Stark Spectra (4/70A&S) and the Two-State 1-Mode Model (2/1A&S) Fitting to the Absorption and Stark Spectra[a]

	ρ_L				ΔE_m (V)				$f\Delta\mu$ (D)				
mutant	obs.[b]	4/70A	4/70A&S	2/1A&S	obs.[c]	4/70A	4/70A&S	2/1A&S	calcd.[d]	4/70A	4/70A&S	2/1A&S	R[e] (Å)
WT(previous)	0.68	0.67		0.66					34			32	7.87
WT	0.68	0.69	0.70	0.70	(0)	(0)	(0)	(0)	41	32	35	32	7.87
L131LH	0.47	0.42	0.37	0.34	0.075	0.074	0.086	0.113	46	25	29	27	7.82
M160LH	0.83	0.88	0.91	0.89	0.070	0.011	0.015	0.027	46	18	21	21	7.85
M160LH/L131LH	0.69	0.70	0.72	0.79	0.118	0.118	0.145	0.168	49	23	27	24	7.86

[a] The spectral simulations do not discriminate between ρ_L and 1-ρ_L; the values most consistent with the experimental data for both ρ_L and ΔE_m are shown. [b] From ref 2, constrained during the spectral predictions based on the WT(previous) analysis[12] [c] From ref 7, the WT(previous) predictions[12] are 0.060 V (L131LH), 0.042 V(M160LH), and 0.121 V (M160LH/L131LH). [d] From DFT calculations for a model BChl-b dimer in C_2 symmetry without the presence of L131 or M160 residues[12] assuming $f = 1.15$. [e] Mg−Mg bond lengths R from simulations of the protein structures.[57]

2/1A&S likely result from the current fitting method, which fits to just the central region in which the model is most reliable, instead of the whole spectrum. The parameter that differs most significantly is E_0^{GS-HT}, increasing by 10 mV (4/70A&S) and 20 mV (2/1A&S), indicating that the precision by which it can be determined is restricted. Significantly, for 2/1A&S, this induces a change from 66% to 70% in ρ_L.

In the first set of calculations for the mutants, the a priori analysis, in which the model parameters are constrained to WT-(previous) except for E_0^{GS-HT}, the predicted absorption spectra are not in good accord with the observed spectra, despite the fact that the predicted Stark spectra are in excellent agreement, as shown in Figure 6. Thus it appears that in some cases this excellent quantitative agreement for the Stark spectra arises from cancellation of errors. Note also that the significant overestimates of the magnitude of the Stark spectra result from using the WT value for $\Delta\mu$ (34 D/f) to calculate the a priori Stark spectra. This indicates that properties other than E_0^{GS-HT} vary with mutations and more model parameters need to be optimized to improve quantitative agreement between the calculated and the observed absorption.

Subsequently in the 4/70A analysis, the six major parameters, J^{GS-HT}, $\lambda^{A,GS-HT}$, E_0^{GS-HT}, $\lambda^{S200,GS-HT}$, $\lambda^{A,HT-SH}$, and E_{SH}, are adjusted to fit the absorption data, and then the Stark spectra are predicted. As shown in Figure 6, this optimization produces quantitative agreement with the absorption spectra, but the agreement with the Stark spectra is not significantly improved over the a priori results for the L131LH and M160LH/L131LH mutants and is significantly degraded for M160LH. A feature of the Stark spectra that is not well reproduced for M160LH and L131LH/M160LH is the location of the zero-crossing near 3000 cm^{-1}, whose frequency is underestimated by as much as 200 cm^{-1}.

To account for both absorption and Stark spectra, the model 4/70A&S is used in which the simulation is constrained to fit both absorption and Stark spectra simultaneously. Significant improvement over earlier models was not found, however, until two additional parameters, $\lambda^{A,SH-HTSH}$ and $E_0^{SH-HTSH}$, were also allowed to vary. Changes to these parameters allow the degree of charge delocalization between the SH and HTSH states to be different from that between the GS and HT states. The spectra were found to be insensitive to the other parameters $\lambda^{A,GS-HTSH}$ and $J^{SH-HTSH}$, and hence these parameters remained fixed to those of the more accessible quantities $\lambda^{A,HT-SH}$ and J^{GS-HT}, respectively. As shown in Figure 2, the locations of the Stark zero-crossing are very sensitive to the degree of charge delocalization, and as the SH absorption strongly overlaps most of the HT absorption, the locations of the zero-crossings become sensitive to $\lambda^{A,SH-HTSH}$ and $E_0^{SH-HTSH}$. Figure 6 shows that the 4/70A&S model fits all spectroscopic properties quantitatively, except for the Stark zero-crossing of L131LH/M160LH, which is in error by 80 cm^{-1}.

For the simpler 2/1A&S model, an excellent agreement between the fitted and observed spectra in the central (ca. 2400−3000 cm^{-1}) region is obtained, as shown in Figure 6, and the fitted parameters are able to predict most of the key qualitative features of the electronic transitions observed outside of the fitting region. A correlation between the model parameters and the predicted spectra can be described as follows: The absorption band maximum is found to be most sensitive to J^{GS-HT}, the absorption bandwidth is found to be most sensitive to the spectral resolution, and the location of the Stark zero-crossing is found to be directly dependent on E_0^{GS-HT}. (Note that the same principles apply to the four-state 70-mode model, but simple conclusions are complicated by the additional electronic states.) The features in the central region are found to be somewhat insensitive to the fourth parameter $\lambda^{A,GS-HTSH}$, making it difficult to obtain a precise value; this parameter determines both the net phase-phonon intensity and the properties of the high-frequency tail, features not included in the fits of the 2/1A&S model. The major assumption limiting the quantitative accuracy of the J^{GS-HT} and E_0^{GS-HT} parameters is the neglect of the SH shoulder. According to perturbation theory, the interaction between the SH and the HT states serves to push the HT band maximum to a higher energy, and this is manifest in Table 4 through a ca. 8% overestimation of J^{GS-HT} by the 2/1A&S model compared to the four-state approaches. Furthermore, this interaction in general pushes the Stark zero-crossing to a higher frequency[5] than it would be otherwise. An attempt to account for this effect using the 2/1A&S model results in overestimation of $|E_0^{GS-HT}|$ by 10−50 meV, associated with overestimations of the degree of charge localization ρ_L by up to 7% as shown in Table 5.

B. Variation of the Asymmetry Parameter E_0^{GS-HT} and the Predicted Spin-Density and Midpoint Potential. In the previous section, it was demonstrated that the Stark spectra provide a sensitive indicator of E_0^{GS-HT}. Here we compare values of E_0^{GS-HT} obtained from fitting the spectra of the mutants to the values of E_0^{GS-HT} obtained from fitting the spin-density distributions and electrochemical midpoint potentials.[12] Conversely, the E_0^{GS-HT} values from the spectral analyses are used to calculate the charge localization and the electrochemical properties for comparison with the observed values. Note that the values of E_0^{GS-HT} determined from the spin-density and electrochemical data should not be thought of as being direct experimental observables as they were obtained[12] using a

complete chemical model[5] for the special-pair radical cation, the model that is actually being refined in this current work. That is, even though E_0^{GS-HT} dominates the effects of mutation on the spin-density and electrochemical data,[9-12] quantitative estimates of it cannot be obtained without using a comprehensive chemical model.[12] The analogous problem is present in the interpretation of the Stark spectra but to a much lesser extent: While the central Stark zero-crossing is controlled primarily by E_0^{GS-HT}, fully quantitative analysis demands the proper treatment of the SH state and its delocalization controller, $E_0^{SH-HTSH}$.

As stated in the previous section, for WT the current fitted value of E_0^{GS-HT} increases by 10−20 meV from that of the WT(previous) parameters set. This change is associated with subtle changes in the observed spectra in the central region and thus should serve as an error estimate for this quantity. For the mutants, significant changes are found between different models used; for example, in the case of L131LH, E_0^{GS-HT} ranges from −11 meV for a priori to −26 meV for 4/70A and to −43 meV for 4/70A&S. In this case, the large differences between models 4/70A and 4/70A&S arise because the absorption spectrum is insensitive to E_0^{GS-HT} when $E_0^{GS-HT} \approx 0$ (a condition which applies for L131LH), while the Stark spectrum remains very sensitive. Note that the sign of E_0^{GS-HT} cannot be uniquely determined from the spectroscopic data, and the signs given in the table are chosen to provide the best agreement with both the observed spin-density and electrochemical data. In general, the degree of asymmetry is increased by model 4/70A&S due to the constraint of fitting the Stark zero-crossing. This effect is enhanced even more in the fits to model 2/1A&S, which omit the SH states. As shown in Table 5, the calculated charge localization thus increases accordingly: ρ_L for M160LH changes from 0.83 (observed) to 0.88 (4/70A) to 0.91 (4/70A&S) to 0.89 (2/1A&S); for L131LH ρ_L changes from 0.47 (the observed value) to 0.42 (4/70A) to 0.37 (4/70A&S) to 0.34 (2/1A&S).

The largest differences between the observed and the deduced electrochemical midpoint potential changes relative to WT, ΔE_m, are found for M160LH: i.e., 70 mV (observed) compared to 42 mV (WT(previous)[12]) to 11 mV (4/70A) to 15 mV (4/70A&S) to 27 mV (2/1A&S). These are large compared to the 3 mV estimated error in the experimental data or the 8 mV error found in the analysis of 25 mutant RCs in which the WT(previous) parameters are determined.[12] Notably, in that study M160LH mutants also exhibit anomalous behavior,[12] and it seems that the values obtained here deviate from the expected behavior to an even greater extent. For the other mutants, smaller but still significant discrepancies between the calculated midpoint potential and the observed values are obtained, as described in Table 5. These discrepancies are further discussed in section VI.

C. Variation of the Electronic Coupling J^{GS-HT}. The fitted values of the electronic coupling J^{GS-HT} show little variation except for M160LH for which it decreases by 20% irrespective of the models used. As shown in Figure 6, the a priori predicted spectra of this mutant, based on the assumption that mutation affects only E_0^{GS-HT}, significantly overestimates the frequency of the HT band;[12] it is necessary to use a reduced value of the electronic coupling to account for this. This variation is suggestive of large-scale effects such as mutation-induced structural changes to the special pair, since an environmental perturbation by the mutation should not have such a direct influence upon the coupling.

D. Variation of the Antisymmetric-Mode Reorganization Energy $\lambda^{A,GS-HT}$. The antisymmetric-mode reorganization energy $\lambda^{A,GS-HT}$ is determined by the internal geometric changes within the special pair associated with oxidation and reduction of its individual bacteriochlorophylls as well as the response of the surrounding environment to these changes.[38] Mutations directly modulate the response of the environment and hence can affect $\lambda^{A,GS-HT}$. However, for the environmental response to have an effect, it must involve processes happening on the ca. 30 fs spectroscopic time scale, a time scale on which typically only the electronic polarization component can respond. As the mutated sites constitute a rather small part of the environment of P^+, their effects on the reorganization energy by this mechanism are not expected to be strong. Alternatively, if the hydrogen bonds between the special pair and the mutated residues are rapidly broken upon excitation, then $\lambda^{A,GS-HT}$ could be increased by up to the value of the hydrogen-bond strength, ca. 0.25 eV, a significant value compared to $\lambda^{A,GS-HT} = 0.14$ eV for WT. Whereas hydrogen-bond breakage upon excitation may be a rapid process, hydrogen-bond formation likely involves extended nuclear motion and is not expected to be rapid enough to contribute to $\lambda^{A,GS-HT}$. With this assumption, changes to $\lambda^{A,GS-HT}$ should provide a direct measure of the nature of the hydrogen bonding of the mutants, a more direct measure in fact than, say, the changes induced to the carbonyl vibration frequency, as this quantity is affected by the changes in both the electric field and the hydrogen bonding itself.

As indicated in Table 4, the fitted values of $\lambda^{A,GS-HT}$ do increase for the mutants. The 4/70A&S model shows increases of 0.044 eV for L131LH, 0.069 eV for M160LH, and 0.018 eV for the double mutant M160LH/L131LH. The increases obtained from the 2/1A&S model are approximately half those predicted by the other approaches, most likely because the model was fitted to the central part of the spectrum that is relatively insensitive to $\lambda^{A,GS-HT}$. All these changes are much less than the full hydrogen-bond strengths, and here it is interpreted in terms of differing natures of the local hydrogen-bond environments, assuming that other contributions to $\lambda^{A,GS-HT}$ are not significantly perturbed in the mutants. This leads to the deduced state of hydrogen bonding for the vertically excited HT as shown in Table 3 and described therein. It must be cautioned that these qualitative descriptions of the hydrogen-bonding states are based primarily on the increase in the fitted parameters of $\lambda^{A,GS-HT}$ relative to the WT and with several assumptions about the nature of $\lambda^{A,GS-HT}$. For M160LH, the charge in P^+ is highly localized on P_L in the GS (Table 5) and so the hydrogen bond to M160 is initially strong. Most of this charge is transferred to P_M upon excitation, however, breaking the hydrogen bond and hence producing the large increase in $\lambda^{A,GS-HT}$. For M160LH/L131LH, the hydrogen bond to P_L is initially broken in the GS, and as this will not reform on the spectroscopic time scale for HT, no contribution to $\lambda^{A,GS-HT}$ is produced from this side of the special pair. On the P_M side, the hydrogen-bonding scenario is analogous to that of M160LH, but its excitation involves only approximately half the charge flow, and hence the changes to the hydrogen bonding are much less, resulting in approximately half the change to $\lambda^{A,GS-HT}$ compared to M160LH. Similarly for L131LH, the hydrogen bond to the 13^1-keto group of P_L is initially weak, presumably due to competitive processes involving the 13^3-ester group. A smaller change in $\lambda^{A,GS-HT}$ is thus expected for L131LH compared to M160LH, as observed.

E. Variation in the Parameters Specifying the SH and HTSH States. The 2200 cm^{-1} shoulder of the main intervalence band is governed by four parameters, $\lambda^{A,HT-SH}$ controlling its absorption intensity, E_{SH} controlling its location, $\lambda^{A,SH-HTSH}$ controlling its width (though obscured under the HT absorption band), and $E_0^{SH-HTSH}$ controlling its delocalization, and hence

its contribution to the Stark spectral profile. These parameters involve the SHOMOs of the BChl, which are expected to follow parallel, though not exactly the same, energetic trends with respect to the HOMOs, which are involved in the main GS−HT transition. Of these, while the first two are not expected to vary with the mutations, the latter two should be affected by the mutations in a manner similar to those for $\lambda^{A,GS-HT}$ and E_0^{GS-HT}. In previous studies[12] and in the a priori and 4/70A calculations, these parameters are fixed at those of the analogous ones for the GS and HT states. These constraints are relaxed with the simultaneous fitting of the absorption and Stark spectra in the 4/70A&S model.

As listed in Table 4, the fitted values of $\lambda^{A,HT-SH}$ vary more than expected, however, reflecting the observed changes in the SH band intensity of ca. 20%. For E_{SH}, no variation is found using the 4/70A or the 4/70A&S model, with the exception of the 4/70A&S fit for M160LH. This could be an indication of the effects associated with structural changes to and around the special pair. For $E_0^{SH-HTSH}$, the fit parameters closely parallel those of E_0^{GS-HT}, as expected. The subtle differences between these two values are likely to be physically realistic estimates since they significantly influence the Stark line shape. For $\lambda^{A,SH-HTSH}$ the fitted values are found to be 2−3 times larger than those of $\lambda^{A,GS-HT}$. Since earlier calculations[35] predict that $\lambda^{A,SH-HTSH}$ should actually be *less* than $\lambda^{A,GS-HT}$, a better characterized analogous property, we consider the fit parameters for $\lambda^{A,SH-HTSH}$ to be unrealistic. One explanation for this is that the observed spectra are not a sensitive indicator of $\lambda^{A,SH-HTSH}$. That is, $\lambda^{A,SH-HTSH}$ influences the SH bandwidth and, through this effect, the Stark line shape. However, this is frustrated by the fact that the bandwidth itself is weakly dependent on $\lambda^{A,SH-HTSH}$ but highly sensitive to other nonoptimized parameters such as the details of the symmetric-mode displacements between the GS and the HT states, whose values are fixed at theoretical values in this study.[35] It is conceivable that a relatively minor change to these parameters could perturb the bandwidth to a greater extent than that caused by $\lambda^{A,SH-HTSH}$, and this suggests one area in which the four-state 70-mode model can be further improved.

F. Changes in Dipole Moment $\Delta\mu$ between the Fully Charge-Localized Diabatic States. For an immobilized isotropic collection of molecules, the intensities of the Stark spectra are proportional to the even power of $|f\mathbf{F}\Delta\mu|$ (primarily $|f\mathbf{F}\Delta\mu|^2$ at experimentally achievable field strengths), since the terms with odd-power dependence on $|f\mathbf{F}\Delta\mu|$ average to zero.[45] As reported in section IV, the quadratic dependence on the electric field strength for P^+ has been experimentally verified. Also, for the parameters set obtained in this study, the simulated Stark spectra (using model 2/1A&S) scale quadratically within the experimentally achievable field strength, although it must be noted that for MVCs in general nonquadratic dependence is possible within the scope of the nonadiabatic theory, in particular for large values of $\Delta\mu$.[4] The values of $\Delta\mu$ for the mutants are determined by scaling the simulated Stark spectra to fit the observed spectra and are given in Table 5. The magnitudes of $\Delta\mu$ are found to be quite independent of the spectroscopic models used in the fitting procedure.

For the WT, the 4/70A&S analysis yields $f\Delta\mu = 35$ D compared to calculated values of $f\Delta\mu = 34$ D obtained from DFT calculations for a model system of the WT[12] and 41 D obtained by applying the same computational procedure to an in situ optimized structure[57] of the special pair. These calculations involve optimizing the structures for the neutral reaction centers, starting from the X-ray crystallographic coordinates and calculating the change in charge distributions on oxidation of one BChl in the absence of the other but in the presence of the nearby residues. Results of similar calculations shown in Table 5 for the mutants predict that $\Delta\mu$ increases due to hydrogen bonding. This effect arises as some of the charge gets delocalized out to the histidines. However, the values of $f\Delta\mu$ determined from the observed spectra are found to decrease significantly in the mutants, from 35 D in WT to 29 D (L131LH), 27 D (M160LH/L131LH), and finally 21 D (M160LH). While such changes are to be expected if a significant shortening of the Mg−Mg distance is involved, the in situ optimized Mg−Mg bond lengths for the neutral states of the mutant reaction centers,[57] as shown in Table 5, indicate minimal change to this distance. These optimizations did not allow for long-range structural rearrangement, and it can be argued that the largest change in $\Delta\mu$ found for M160LH implies the presence of a structural change. However, along this line of reasoning a change of ca. 20% shortening of the Mg−Mg distance would be required to interpret $\Delta\mu$ for L131LH and M160LH/L131LH. This change would lead to a drastic alteration of the properties of these species, for example, a significant change in the electronic coupling J^{GS-HT}. This has not been observed, however, and as has been discussed in the previous sections, the parameters determined for these two species are reasonably close to a priori expectations based on the WT(previous) parameters[12] so as to preclude this possibility.

The magnitude of $\Delta\mu$ is directly related to the effective distance of charge displacement. This quantity is expected to correspond to a value close to the center-to-center distance. For the systems studied here, the reduction in $\Delta\mu$ appears larger than could be accounted for solely by shortening the center-to-center distance of BChls. Another mechanism that could be involved is the effect of the electric field from the engineered histidine. This could polarize the BChls to reduce $\Delta\mu$ or alter the electronic charge distributions to a greater extent than or with the opposite direction from that predicted by the calculation. In this view, the mutations amount to a specific change in the first solvation shell of the radical cation, in which the resulting effects on the energetics and the configurations of the BChl orbitals are not limited to just altering the potential energies of the diabatic states. For simpler conjugated systems such as donor/acceptor polyenes,[60,61] a significant reduction of $\Delta\mu$ due to the changes in the solvent environment (from nonpolar toluene to polar aprotic 2-methyltetrahydrofuran) has been previously observed. If the mutations affected the electronic structure of the special radical cation more extensively than predicted by calculations, this should also be reflected in other spectroscopic transitions. Indeed, a shift in the frequency of the tripdoublet bands for the hydrogen-bond mutants have been observed,[62] as described in the next section.

VI. Comparison of the Fit Parameters to Previously Estimated Properties of P^+

When compared to the experimental values for the charge-delocalization and the electrochemical midpoint potentials,[2,7−9] the parameters obtained from fitting the observed spectra generally conform to the observed trend, while exhibiting some quantitative variations, as summarized in subsection V.B. It must be noted that the experimental conditions for the absorption/Stark experiments differ from those of the ENDOR and electrochemical experiments. The absorption and Stark spectra (and also the X-ray structure, which forms the basis of the structure−function insights for the RCs) were measured at cryogenic temperature, whereas the electrochemical and EN-

DOR measurements are performed at close to room temperature. Another point of difference is the detergent in which the RCs are solubilized. In the ENDOR and electrochemical experiments,[2,7−9] the RCs are solubilized in the zwitterionic detergent lauryldimethylamine oxide (LDAO), whereas in this study, the RCs are solubilized in Triton X-100, a nonionic detergent. A specific effect of detergents has been reported for WT in which a major conformational change is induced by ionic detergents as measured by the change of the spin localization from $\rho_L = 0.68$ to 0.85.[63] However, this particularly drastic effect is not expected to apply here, since the nonionic Triton detergent is generally believed to be milder and less disruptive to the protein than LDAO. Nevertheless, differences in at least the hydrogen-bonding patterns can result from the difference in the solubilization condition, i.e., between the native chromatophore lipid bilayer[17] and the detergent micelles studied here. Another important factor is the difference in the sample preparation techniques; the RCs for FTIR spectroscopy are prepared as dehydrated films, while the spin-density[2] and midpoint-potential[7] measurements are performed in an aqueous environment. As noted earlier in section IV, the degree of hydration is known to modulate the absorption and Stark spectra[28] of P^+, with the band shifting toward the low energy by a few tens of cm^{-1}. Thus, it is quite likely that the properties determined from fitting to the spectra of the dehydrated film differ from the properties of fully hydrated RCs. Finally, it must also be noted that while absorption and Stark spectroscopy probe the system on the ultrafast time scale of excitation, the electrochemical and ENDOR measurements involve a considerably longer time scale and thus can be considered equilibrium measurements.

For L131LH and M160LH/L131LH, these factors could account for most of the discrepancies in the values of ρ_L and ΔE_m between the two approaches. For M160LH, however, the properties determined from the spectra deviate from expected values of the parameters to a much greater extent, with large decreases in $\Delta\mu$ (by ca. 40%) and J^{GS-HT} (ca. 20%), a decrease in ΔE_m by 45mV, and a very strong charge localization on P_L ($\rho_L = 91\%$ versus the observed value of 83%). This is reflected in the striking differences between the observed and the a priori predicted absorption spectrum of M160LH: Its HT transition energy is anomalously low,[12] its phase-phonon lines are too intense, and the central region of the band is much broader than expected.

One possible explanation for the differences observed for M160LH could be the limitations of the spectroscopic model. Certain model parameters, such as the specification of the vibrational modes, are fixed to the results from a DFT calculation for WT,[35] not being optimized for the mutants. However, similar fit parameters are obtained from the two-state 1-mode model, which includes only a single antisymmetric mode; thus it appears unlikely that the details of the vibrational specifications are responsible for the deviations. A more likely scenario is that a structural change happens in M160LH as a result of the hydrogen bonding, possibly associated with subtle changes in the electronic structures. The departure from expected behavior for the M160LH mutant has been noted in previous experimental and theoretical studies,[12,62,64] and it is quite plausible that the current experimental conditions further accentuate these changes. For example, the Q_y absorption and Stark spectra for M160LH are significantly different from the WT,[64] even though those of L131LH and M160LH/L131LH are quite similar. Furthermore, the intensity of the tripdoublet band is dramatically reduced.[62] The tripdoublet band can be thought of as the singlet−triplet transition on the "neutral" half of the dimer and, like the HT band, derives its intensity from the inter-BChl coupling within the special pair. The results for J^{GS-HT} shown in Table 4, which indicate that the coupling is significantly lowered in M160LH compared to WT, L131LH, and M160LH/L131LH, are consistent with the observed reduction in the tripdoublet band intensity.[25] Furthermore, a downshift in the frequencies of the tripdoublet bands for the mutants are also observed to correlate with hydrogen bonding to the 13^1-keto group. These changes in the transition frequencies are observed for both M160LH and L131LH as well as for M160LH/L131LH, for which the shift is nearly twice the shift in the single mutant. This is suggestive of a perturbation in the electronic structure of the mutant P^+ relative to WT. It can be speculated that these are related to the observed anomalies in the properties of M160LH and to a lesser extent, $\Delta\mu$, for L131LH and M160LH/L131LH. However, further experimental and theoretical studies on the tripdoublet transition will be necessary to answer these questions.

VII. Conclusion

In this work, we have observed drastic changes in the Stark line shapes of the mid-IR intervalence charge-transfer bands of the special-pair cation associated with mutations in the vicinity of P. Through nonadiabatic simulations, these changes are determined to be induced by the changes in the energy asymmetry E_0^{GS-HT}, with smaller contributions from other parameters, most notably the reorganization energy $\lambda^{A,GS-HT}$. In the case of the M160LH mutant, it is revealed that changes in several parameters are more extensive, notably with a sizable decrease in the electronic coupling J^{GS-HT}; these are attributed to a larger degree of structural changes in the special pair, as has also been suggested in earlier studies on this mutant.[12,62] In our earlier work[4] with nonadiabatic simulations, we have predicted such drastic changes in the Stark spectra as a function of the energy asymmetry. This prediction appears to be borne out in the observations reported here, verifying the appropriateness of the nonadiabatic model for the spectroscopy of P^+. Specifically for Stark spectroscopy of MVCs, this study supports our prior assertion that the nonadiabatic approach is more suitable than the Liptay model,[4,33] especially for the intermediate to strong coupling regime, which has been a subject of much interest in recent times. We have employed two implementations of the nonadiabatic model, which differ in the number and nature of the vibrational modes included. It is demonstrated that both implementations agree well on key parameters such as the electronic coupling, the energy asymmetry, and $\Delta\mu$, indicating the robustness of the model and suggesting that it would be of general utility in characterizing MVCs.

Acknowledgment. This work is supported by the National Science Foundation Biophysics and Chemistry Programs (to S.G.B.), the Australian Research Council, and the Australian Center for Advanced Computing and Communications. P.K. is supported by a Howard Hughes Medical Institute Predoctoral Fellowship and a Stanford Graduate Fellowship. T.P.T. was supported by a Hertz Foundation Predoctoral Fellowship.

Appendix

The Liptay sum-of-derivatives expression for the Stark spectra of isotropic, immobilized samples is

$$\Delta A(\tilde{\nu}) = F^2\left\{A_\chi A(\tilde{\nu}) + \frac{B_\chi}{15hc}\,\tilde{\nu}\,\frac{\mathrm{d}}{\mathrm{d}\tilde{\nu}}\left(\frac{A(\tilde{\nu})}{\tilde{\nu}}\right) + \frac{C_\chi}{30h^2c^2}\,\tilde{\nu}\,\frac{\mathrm{d}}{\mathrm{d}\tilde{\nu}^2}\left(\frac{A(\tilde{\nu})}{\tilde{\nu}}\right)\right\}$$

with

$$A_\chi = \frac{1}{30|\vec{m}|^2}\sum_{ij}[10A_{ij}^{\ 2} + (3\cos^2\chi - 1)(3A_{ii}A_{jj} + A_{ij}^{\ 2})] + \frac{1}{15|\vec{m}|^2}\sum_{ij}[10m_iB_{ijj} + (3\cos^2\chi - 1)(4m_iB_{ijj})]$$

$$B_\chi = \frac{5}{2}\mathrm{Tr}(\Delta\alpha) + (3\cos^2\chi - 1)\left(\frac{3}{2}\Delta\alpha_m - \frac{1}{2}\mathrm{Tr}(\Delta\alpha)\right) + \frac{1}{|\vec{m}|^2}\sum_{ij}[10m_iA_{ij}\Delta\mu_j + (3\cos^2\chi - 1)(3m_iA_{jj}\Delta m_i + m_iA_{ij}\Delta\mu_j)]$$

and

$$C_\chi = |\Delta\mu|^2\cdot[5 + (3\cos^2\chi - 1)(3\cos^2\zeta_A - 1)]$$

where χ denotes the angle between the polarization of the probe beam and the applied electric field, ζ_A denotes the angle between the transition dipole moment ($\vec{m}$) and the difference dipole ($\Delta\mu$), $\vec{m}(\vec{F}) = \vec{m} + A\cdot\vec{F} + \vec{F}\cdot B\cdot\vec{F}$, and $\Delta\alpha_m = (\vec{m}\Delta\alpha\vec{m})/|\vec{m}|^2$.

References and Notes

(1) Hoff, A. J.; Deisenhofer, J. *Phys. Rep.* **1997**, *287*, 1.
(2) Rautter, J.; Lendzian, F.; Schulz, C.; Fetsch, A.; Kuhn, M.; Lin, X.; Williams, J. C.; Allen, J. P.; Lubitz, W. *Biochemistry* **1995**, *34*, 8130.
(3) Reimers, J. R.; Hush, N. S. *Chem. Phys.* **1996**, *208*, 177.
(4) Treynor, T. P.; Boxer, S. G. *J. Phys. Chem. A* **2004**, *108*, 1764.
(5) Reimers, J. R.; Hush, N. S. *J. Chem. Phys.* **2003**, *119*, 3262.
(6) Reimers, J. R.; Hush, N. S. *Chem. Phys.* **2004**, *299*, 79.
(7) Artz, K.; Williams, J. C.; Allen, J. P.; Lendzian, F.; Rautter, J.; Lubitz, W. *Proc. Natl. Acad. Sci. U.S.A.* **1997**, *94*, 13582.
(8) Ivancich, A.; Artz, K.; Williams, J. C.; Allen, J. P.; Mattioli, T. A. *Biochemistry* **1998**, *37*, 11812.
(9) Muh, F.; Lendzian, F.; Roy, M.; Williams, J. C.; Allen, J. P.; Lubitz, W. *J. Phys. Chem. B* **2002**, *106*, 3226.
(10) Johnson, E. T.; Muh, F.; Nabedryk, E.; Williams, J. C.; Allen, J. P.; Lubitz, W.; Breton, J.; Parson, W. W. *J. Phys. Chem. B* **2002**, *106*, 11859.
(11) Reimers, J. R.; Hughes, J. M.; Hush, N. S. *Biochemistry* **2000**, *39*, 16185.
(12) Reimers, J. R.; Hush, N. S. *J. Am. Chem. Soc.* **2004**, *126*, 4132.
(13) Taguchi, A. K. W.; Stocker, J. W.; Alden, R. G.; Causgrove, T. P.; Peloquin, J. M.; Boxer, S. G.; Woodbury, N. W. *Biochemistry* **1992**, *31*, 10345.
(14) Stocker, J. W.; Taguchi, A. K. W.; Murchison, H. A.; Woodbury, N. W.; Boxer, S. G. *Biochemistry* **1992**, *31*, 10356.
(15) Williams, J. C.; Alden, R. G.; Murchison, H. A.; Peloquin, J. M.; Woodbury, N. W.; Allen, J. P. *Biochemistry* **1992**, *31*, 11029.
(16) Breton, J.; Nabedryk, E.; Parson, W. W. *Biochemistry* **1992**, *31*, 7503.
(17) Nabedryk, E.; Allen, J. P.; Taguchi, A. K. W.; Williams, J. C.; Woodbury, N. W.; Breton, J. *Biochemistry* **1993**, *32*, 13879.
(18) Breton, J.; Nabedryk, E.; Clerici, A. *Vib. Spectrosc.* **1999**, *19*, 71.
(19) Rautter, J.; Gessner, C.; Lendzian, F.; Lubitz, W.; Williams, J. C.; Murchison, H. A.; Wang, S.; Woodbury, N. W.; Allen, J. P. EPR and ENDOR studies of the primary donor cation radical in native and genetically modified bacterial reaction centers. In *The Photosynthetic Bacterial Reaction Center II: Structure, Spectroscopy, and Dynamics*; Jacques Breton, J., Verméglio, A., Eds.; NATO ASI Series, Series A, Life Sciences 237; Plenum Press: New York, 1992; p 99.
(20) Lin, X.; Murchison, H. A.; Nagarajan, V.; Parson, W. W.; Allen, J. P.; Williams, J. C. *Proc. Natl. Acad. Sci. USA* **1994**, *91*, 10265.
(21) Ermler, U.; Fritzsch, G.; Buchanan, S. K.; Michel, H. *Structure* **1994**, *2*, 925.
(22) Deisenhofer, J.; Epp, O.; Miki, K.; Huber, R.; Michel, H. *Nature* **1985**, *318*, 618.
(23) Michel, H.; Epp, O.; Deisenhofer, J. *EMBO J.* **1986**, *5*, 2445.
(24) Feher, G.; Allen, J. P.; Okamura, M. Y.; Rees, D. C. *Nature* **1989**, *339*, 111.
(25) Reimers, J. R.; Hush, N. S. *J. Am. Chem. Soc.* **1995**, *117*, 1302.
(26) Reimers, J. R.; Shapley, W. A.; Hush, N. S. *J. Chem. Phys.* **2003**, *119*, 3240.
(27) Hammes, S. L.; Mazzola, L.; Boxer, S. G.; Gaul, D. F.; Schenck, C. C. *Proc. Natl. Acad. Sci. U.S.A.* **1990**, *87*, 5682.
(28) Treynor, T. P.; Andrews, S. S.; Boxer, S. G. *J. Phys. Chem. B* **2003**, *107*, 11230.
(29) Oh, D. H.; Sano, M.; Boxer, S. G. *J. Am. Chem. Soc.* **1991**, *113*, 6880.
(30) Stocker, J. W.; Hug, S.; Boxer, S. G. *Biochim. Biophys. Acta* **1993**, *1144*, 325.
(31) Middendorf, T. R.; Mazzola, L. T.; Lao, K. Q.; Steffen, M. A.; Boxer, S. G. *Biochim. Biophys. Acta* **1993**, *1143*, 223.
(32) Zhou, H. L.; Boxer, S. G. *J. Phys. Chem. B* **1998**, *102*, 9139.
(33) Reimers, J. R.; Hush, N. S. Electric field perturbation of electronic (vibronic) absorption envelopes: Application to characterization of mixed-valence states. In *Mixed Valency Systems: Applications in Chemistry, Physics, and Biology*; Prassides, K., Ed.; Kluwer Academic Publishers: Dordrecht, The Netherlands, 1991; p 29.
(34) Reimers, J. R.; Hutter, M. C.; Hughes, J. M.; Hush, N. S. *Int. J. Quantum Chem.* **2000**, *80*, 1224.
(35) Reimers, J. R.; Shapley, W. A.; Rendell, A. P.; Hush, N. S. *J. Chem. Phys.* **2003**, *119*, 3249.
(36) Rice, M. J.; Yartsev, V. M.; Jacobsen, C. S. *Phys. Rev. B* **1980**, *21*, 3437.
(37) Allen, G. C.; Hush, N. S. *Prog. Inorg. Chem.* **1967**, *8*, 357.
(38) Hush, N. S. *Prog. Inorg. Chem.* **1967**, *8*, 391.
(39) Creutz, C.; Taube, H. *J. Am. Chem. Soc.* **1969**, *91*, 3988.
(40) Reimers, J. R.; Hush, N. S. *Inorg. Chim. Acta* **1994**, *226*, 33.
(41) Reimers, J. R.; Hush, N. S. *Chem. Phys.* **1995**, *197*, 323.
(42) Takiff, L.; Boxer, S. G. *J. Am. Chem. Soc.* **1988**, *110*, 4425.
(43) Piepho, S. B.; Krausz, E. R.; Schatz, P. N. *J. Am. Chem. Soc.* **1978**, *100*, 2996.
(44) Fischer, G. *Vibronic Coupling*; Academic Press: London, 1984.
(45) Bublitz, G. U.; Boxer, S. G. *Annu. Rev. Phys. Chem.* **1997**, *48*, 213.
(46) Lockhart, D. J.; Boxer, S. G. *Biochemistry* **1987**, *26*, 664.
(47) Reimers, J. R.; Hush, N. S. *J. Phys. Chem.* **1991**, *95*, 9773.
(48) Oh, D. H.; Boxer, S. G. *J. Am. Chem. Soc.* **1990**, *112*, 8161.
(49) Bublitz, G. U.; Laidlaw, W. M.; Denning, R. G.; Boxer, S. G. *J. Am. Chem. Soc.* **1998**, *120*, 6068.
(50) Lockhart, D. J.; Hammes, S. L.; Franzen, S.; Boxer, S. G. *J. Phys. Chem.* **1991**, *95*, 2217.
(51) Zhou, H. L.; Boxer, S. G. *J. Phys. Chem. B* **1998**, *102*, 9148.
(52) Goldsmith, J. O.; King, B. A.; Boxer, S. G. *Biochemistry* **1996**, *35*, 2421.
(53) Paddock, M. L.; Rongey, S. H.; Feher, G.; Okamura, M. Y. *Proc. Natl. Acad. Sci. U.S.A.* **1989**, *86*, 6602.
(54) Andrews, S. S.; Boxer, S. G. *Rev. Sci. Instrum.* **2000**, *71*, 3567.
(55) Andrews, S. S.; Boxer, S. G. *Appl. Spectrosc.* **2001**, *55*, 1161.
(56) Okamura, M. Y.; Feher, G. *Annu. Rev. Biochem.* **1992**, *61*, 861.
(57) Hughes, J. M.; Hutter, M. S.; Reimers, J. R.; Hush, N. S. *J. Am. Chem. Soc.* **2001**, *123*, 8550.
(58) Shreve, A. P.; Cherepy, N. J.; Franzen, S.; Boxer, S. G.; Mathies, R. A. *Proc. Natl. Acad. Sci. U.S.A.* **1991**, *88*, 11207.
(59) Mantele, W.; Nabedryk, E.; Tavitian, B. A.; Kreutz, W.; Breton, J. *FEBS Lett.* **1985**, *187*, 227.
(60) Bublitz, G. U.; Ortiz, R.; Marder, S. R.; Boxer, S. G. *J. Am. Chem. Soc.* **1997**, *119*, 3365.
(61) Bublitz, G. U.; Ortiz, R.; Runser, C.; Fort, A.; Barzoukas, M.; Marder, S. R.; Boxer, S. G. *J. Am. Chem. Soc.* **1997**, *119*, 2311.
(62) Mattioli, T. A.; Lin, X.; Allen, J. P.; Williams, J. C. *Biochemistry* **1995**, *34*, 6142.
(63) Muh, F.; Rautter, J.; Lubitz, W. *Biochemistry* **1997**, *36*, 4155.
(64) Moore, L. J.; Zhou, H. L.; Boxer, S. G. *Biochemistry* **1999**, *38*, 11949.